

Highlights

On applicability of von Karman's momentum theory in predicting the water entry load of V-shaped structures with varying initial velocity

Yujin Lu, Alessandro Del Buono, Tianhang Xiao, Alessandro Iafrati, Shuanghou Deng, Jinfu Xu

- The maximal acceleration is proportional to the square of the initial velocity for the V-shaped body
- The theoretical ratio of the corresponding velocity to the initial velocity is valid for large impact velocity
- Gravity effect should be considered with slow impact speed
- A coupled relation among $a_{z\max}$, v_z^* and z^* is found

On applicability of von Karman's momentum theory in predicting the water entry load of V-shaped structures with varying initial velocity

Yujin Lu^{a,b}, Alessandro Del Buono^{b,*}, Tianhang Xiao^{a,**}, Alessandro Iafrati^b, Shuanghou Deng^a and Jinfa Xu^a

^aNanjing University of Aeronautics and Astronautics, Yudao Street 29, Nanjing, 210016, Jiangsu, People's Republic of China

^bNational Research Council-Institute of Marine Engineering (CNR-INM), Via di Vallerano 139, Roma, 00128, Lazio, Italy

ARTICLE INFO

Keywords:

water landing
amphibious aircraft
momentum theory
acceleration
linear dependence

ABSTRACT

The water landing of an amphibious aircraft is a complicated problem that can lead to uncomfortable riding situation and structural damage due to large vertical accelerations and the consequent dynamic responses. The problem herein is investigated by solving unsteady incompressible Reynolds-averaged Navier-Stokes equations with a standard $k - \omega$ turbulence closure model. The theoretical solutions established by the von Karman's momentum theory are also employed. In order to validate the relationships between the initial vertical velocity and the peak value of vertical acceleration, free fall test cases of 2D symmetric wedge oblique entry and 3D cabin section vertical entry are presented first. The other parameters at which the maximum acceleration occurs, such as time, penetration depth, velocity, are also evaluated. Hence, the quantitative relations are investigated to water landing event for amphibious aircraft. Detailed results in terms of free surface shape and pressure distribution are provided to show the slamming effects. The results show that a linear dependence of the maximal acceleration from the square of initial vertical velocity can be derived for two-dimensional wedge, three-dimensional cabin section and seaplane with V-shaped hull. Moreover, the ratio between the corresponding velocity and the initial vertical velocity tends to a constant threshold value, 5/6, derived from the theoretical solution, when increasing the initial vertical velocity in all three cases.

© 2022. This manuscript version is made available under the CC-BY-NC-ND 4.0 license <https://creativecommons.org/licenses/by-nc-nd/4.0/>

Nomenclature

α	velocity angle, °
α_w	volume fraction of water
β	deadrise angle, °
ω	angular velocity of the object, rad/s
L	tensor of the moments of inertia, kg·m ²
M	resultant moment acting on the object, N·m
κ	the ratio of the corresponding velocity to the initial velocity
θ	the heel angle, °
v, v_0	velocity and the initial velocity, m/s
ζ	resultant displacement, m

*Corresponding author

**Corresponding author

 alessandro.delbuono@inm.cnr.it (A.D. Buono); xthang@nuaa.edu.cn (T. Xiao)

ORCID(s):

a_{\max}	non-dimensional maximal acceleration
a_x, a_z	non-dimensional acceleration in x - and z -direction
b	intercept
C_p	pressure coefficient
$F_{\text{hd}}^*, F_{\text{hs}}^*$	maximal vertical hydrodynamic and hydrostatic force, N
k	slope
L	length of the cabin and the fuselage, m
M	mass, kg
m_{added}	added mass, kg
V, V_w	the volume of the cell and the volume of water in the cell, m^3
W	width, m
x_{shift}	shifted coordinate in x -axis, m
z	penetration depth, m
aero	aerodynamic
w, a	water and air

1. Introduction

Amphibious aircraft is a special flight vehicle that is capable of taking off and landing both on water and conventional runways (Qiu and Song, 2013). The amphibious aircrafts have drawn considerable attentions by the nations with maritime supremacy due to their potential military and civilian applications. In the flight operational envelope of amphibious aircraft, landing on water is regarded as the most dangerous phase where the hydrodynamic impact load significantly influences the occupants survivability and structural integrity (Hughes et al., 2013). In terms of the design and analysis of water entry load, full scale tests are regarded as the most straightforward and reliable way. Investigating the hydrodynamics of the water landing of an amphibious aircraft with full scale test are highly expensive and time demanding and, may be challenged by a low repeatability level. In order to derive reliable estimates of the hydrodynamic loads acting on the aircraft during water landing, another practicable way is to perform scaled-model experiments in water basins. As an example, experimental studies on the water entry problems have been conducted at NACA Langley Memorial Aeronautical Laboratory, resulting in extensive and valuable archived test data and recommendations in industrial applications (Benson and Bidwell, 1945). The study provides interesting information about the effects on performances of design parameters such as deadrise angle, depth of step, configuration of hull body, hydrofoils, etc. In general, hydrodynamics of water impacting can be demonstrated commendably by scaled model water tank tests. In the case of seaplanes, both hydrodynamics and aerodynamic aspects play the same key roles in the dynamic behavior and there is however a difficulty in achieving the correct scaling for the air and water domains (Duan et al., 2019). Froude (Fr) scaling guarantees the correct reproduction of the ratio between the inertia and gravity force in the water domain but it do not allow to preserve the Reynolds (Re) similarity and thus the correct scaling of the viscous effects which are important in both water and, especially, in air for the aerodynamic lift and drag (Terziev et al., 2022; Iafrati and Grizzi, 2019). Depending on the full-scale speed, other phenomena like cavitation and ventilation might be also relevant in the water domain that would not be properly reproduced in scaled model tests based on Froude similarity only (Iafrati and Grizzi, 2019).

As an alternative to expensive experimental campaign, the recent developed computational approaches allow to simulate the hydro- and aero- dynamics and kinematic motion of amphibious aircraft in full scale. Different phases during the whole process, such as takeoff/landing, skiing, and other serious situations were investigated recently by numerical simulation. For the takeoff process, (Qiu and Song, 2013) proposed a decoupled algorithm to investigate

the kinematic characteristics, whereby the aerodynamic forces of the full configuration and the hydrodynamic forces of the hull body were computed separately. The whole process was divided into a number of small time-step, and the forces were calculated at each time step. In (Duan et al., 2019) evaluated the porpoising motion, an unstable oscillation phenomenon that threatens the flying safety of amphibious aircrafts, by using a two-phase flow solver in OpenFOAM. Both slipstream caused by the propeller and external forces, viz. thrust and elevator forces, were taken into consideration as well. Results highlighted the important role played by the hydrodynamic force on the heaving and pitching oscillations, while the aerodynamic forces have a rather marginal effect. Similar to the water landing scenarios of amphibian aircraft, ditching events of conventional aircrafts show the same fluid dynamics phenomena, and have been numerically studied widely. The effects of initial pitching angle and velocity (Xiao et al., 2021b; Guo et al., 2013; Qu et al., 2016; Zheng et al., 2021), fluid-structure interaction (Hughes et al., 2013; Siemann et al., 2017; Yang et al., 2020), wave conditions (Woodgate et al., 2019; Xiao et al., 2021a) and various numerical strategies (Bisagni and Pigazzini, 2017; Siemann and Langrand, 2017; Xiao et al., 2017) on the kinematic characteristics and fluid dynamics phenomena have attracted most of the attention. The vertical acceleration, and its peak value in particular, is even more relevant than other kinematic characteristics as it may be responsible for possible comfort and safety problems occur on crew members, besides, of course, the effects in terms of structural integrity of the fuselage once it strikes the water (Neuberg and Drimer, 2017).

The ditching event, it is usually distinguished in four phases: approach, impact, landing, and flotation (Siemann et al., 2017). The impact phase is the most important one in terms of complex fluid-structure interaction. Von Karman (von Karman, 1929) first proposed an analytical estimation method based on a wedge-shaped water impact and introduced the method to settle the impact loads on seaplanes. Subsequently, a number of researches related to water impact have been carried out based on theoretical, computational or experimental approaches (Wagner, 1932; Zhao and Faltinsen, 1993; Scolan and Korobkin, 2001; Korobkin, 2004; Korobkin and Scolan, 2006; Wu and Sun, 2014; Breton et al., 2020; Zekri et al., 2021). It has been shown that, in the case of free-fall, the structure experiences a rapid change of vertical acceleration and velocity, which is similar to what happens in the impact phase of the water landing (Wang et al., 2015). Several studies have focused on the relationship between the maximum acceleration and initial parameters on free-fall water entry. Among these studies, (Gong et al., 2009) simulated a series of cases with various initial entering velocity of the wedge through a Smoothed Particle Hydrodynamics (SPH) model, and relations for the maximum force on the wedge and the corresponding time in terms of the initial entering velocity of the wedge have been directly expressed by fitting formulas for Froude number greater than 2. In the work of (Abraham et al., 2014), the drag-coefficient of a sphere impacting the water surface was found to be independent of some investigated quantities, like the sphere velocity, surface tension, flow regime (laminar or turbulent) and Reynolds number. Hence, algebraic expressions of the drag coefficient versus the dimensionless depth have been established by two fitted polynomials. Effects of parametric variation, such as impact velocity, radius, and mass of the sphere on the impact force and the acceleration, have also been analyzed by (Yu et al., 2019). The peak value of the non-dimensional impact force has been found to be independent of the velocity and the radius, whereas it depends on the mass of sphere. In parallel, simplified expressions for the maximal force and acceleration have been obtained through fitting the relations between the peak value of the non-dimensional force and the non-dimensional mass. The relationships derived in (Yu et al., 2019) have also been mentioned by other researchers' work (Iafrazi and Grizzi, 2019; Iafrazi, 2016; Wen et al., 2020; Wang et al., 2021a; Sheng et al., 2022). However, it is worth noting that only fitting functions of force and acceleration were discussed in the previous studies, whereas the detailed theoretical basis with related relationships have not been derived yet.

The present study is dedicated to numerical simulations of a two-dimensional symmetric wedge and a three-dimensional cabin section in free fall water entry in order to investigate and build up parametric relations, based on the transformation of the von Karman's momentum theory, that can provide the maximal vertical acceleration and the corresponding vertical velocity, penetration depth and time. Particular attention is paid at the effects of horizontal velocity, and three-dimensional flow. The relations are then used to predict the load acting on amphibious aircraft during the water landing. The present work is organized as follows. Section 2 presents the methodology for the theoretical and numerical approaches, and describes the models and the computational setup; the main results are reported and discussed in Sec. 3; final conclusions are drawn in Sec. 4.

77 2. Methodology and Computational Setup

78 2.1. Von Karman's theoretical method and transformation

Pioneer research in water entry problem has been conducted by von Karman (von Karman, 1929), based on momentum theorem and the added mass for the prediction of the hydrodynamic load during the water entry of a V-shaped body penetrating into the water. By applying the momentum conservation at the beginning of the impact and the generic time t , it is obtained,

$$M v_0 = (M + m_{\text{added}}) \cdot v(t) \quad (1)$$

79 where M is the mass of the wedge per unit length, v_0 is the initial vertical impact velocity, $v(t)$ is the instantaneous
80 velocity during the impact. In equation (1), m_{added} is the added mass which is computed by using the flat-plate
81 approximation (see Fig. 1). It is assumed that the added mass is equal to the mass of a half disk of water of radius
82 $r(t)$, which results into $m_{\text{added}} = (\pi \rho r^2(t))/2$ (Mei et al., 1999). In such approximation the effect of the water pile-up
83 is ignored.

With such an assumption, the velocity of the body can be retrieved as:

$$v(t) = \frac{M v_0}{M + m_{\text{added}}} = \frac{M v_0}{M + \frac{\pi \rho z^2(t)}{2 \tan^2(\beta)}} = \frac{2M \tan^2(\beta) v_0}{2M \tan^2(\beta) + \pi \rho z^2(t)} \quad (2)$$

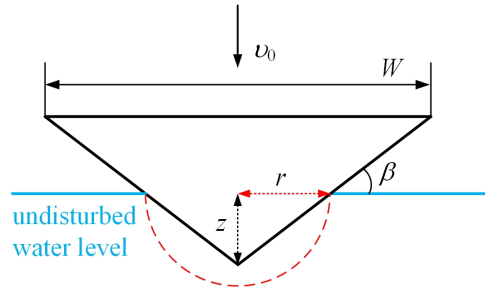


Figure 1: Von Karman's momentum approach.

Based on what is provided in the A and differentiating Eq. (2), it is possible to analytically derive the instantaneous acceleration as follows (Panciroli et al., 2013):

$$a(t) = \frac{\pi \rho z(t)}{M v_0 \tan^2(\beta)} \cdot v^3(t) \quad (3)$$

which takes a peak of magnitude:

$$a^* = v_0^2 \left(\frac{5}{6}\right)^3 \frac{1}{\tan(\beta)} \sqrt{\frac{2\pi\rho}{5M}} \quad (4)$$

when the corresponding penetration depth and velocity are:

$$\begin{cases} z^* = \sqrt{\frac{2M}{5\pi\rho}} \tan(\beta) \\ v^* = \frac{5}{6} v_0 \end{cases} \quad (5)$$

It should be noticed that we define the positive direction of acceleration upwards, while the vertical velocity and penetration depth are positive downwards. Moreover, according to (Panciroli et al., 2013) and (Iafrazi et al., 2000), the corresponding time t^* can be expressed as:

$$t^* = \frac{1}{v_0} \frac{16}{15} \sqrt{\frac{2M}{5\pi\rho}} \tan(\beta) \quad (6)$$

84 Note that the superscript * indicates the values the different quantities take when the acceleration reaches its peak. It is
 85 interesting to notice that a^* , v^* and t^* , are proportional to v_0^2 , v_0 and v_0^{-1} respectively, implying that the initial vertical
 86 velocity governs those parameters, except z^* .

87 2.2. Numerical method

88 In order to numerically simulate the problem, the commercial package Star CCM+ is utilized herein as the two-
 89 phase flow solver. In the present study the unsteady incompressible Reynolds-averaged Navier-Stokes equations with
 90 a standard $k - \omega$ two-equation turbulence model are solved by the finite volume method. The Semi-Implicit Pressure
 91 Linked Equations (SIMPLE) algorithm is employed to achieve an implicit coupling between pressure and velocity,
 92 and the gradient is reconstructed with the Green-Gauss Node Based method. The modified High Resolution Interface
 93 Capturing (HRIC) scheme is adopted for volume fraction transport. The convection terms, as well as diffusion terms,
 94 are turned into algebraic parameters using second-order upwind and second-order central methods, respectively. The
 95 unsteady terms are discretized in the time domain by applying a second-order implicit scheme.

Volume of fluid (VOF) scheme, originally proposed by Hirt and Nichols (Hirt and Nichols, 1981), is used in
 the present computational scheme to capture the water-air interface by introducing a variable, α_w , called the volume
 fraction of the water in the computational cell, which varies between 0 (air) and 1 (water) and is defined as:

$$\alpha_w = V_w/V, \quad (7)$$

where V_w is the volume of water in the cell and V is the volume of the cell. The volume fraction of the air in a cell can
 be computed as:

$$\alpha_a = 1 - \alpha_w. \quad (8)$$

The effective value φ_m of any physical properties, such as density, viscosity, etc., of the mixture of water and air in the
 transport equations is determined by:

$$\varphi_m = \varphi_w \alpha_w + \varphi_a (1 - \alpha_w). \quad (9)$$

To accurately capture the dynamic behavior as well as the load characteristics of water landing process, the motion
 of the body in response to the fluid forces and moments at the surface is determined via a six degree-of-freedom (6DOF)
 model. The 6DOF model solves the equations for the rotation and translation of the center of mass of the object. The
 equation for the translation in the global inertial coordinate system is formulated as:

$$M \cdot \frac{d\mathbf{v}}{dt} = \mathbf{F}, \quad (10)$$

and the rotation of the object is solved in the body local coordinate system by:

$$\mathbf{L} \frac{d\boldsymbol{\omega}}{dt} + \boldsymbol{\omega} \times \mathbf{L}\boldsymbol{\omega} = \mathbf{M}. \quad (11)$$

96 Subsequently, a dynamic mesh strategy (Xiao et al., 2021a), which moves the entire mesh rigidly along with the
 97 object at each time step according to the solution of the 6DOF model, is employed to deal with the relative motion
 98 between the fluid and the rigid body with on single grid domain. As neither mesh distortion nor mesh reconstruction
 99 occurs, the high quality of the initial mesh remains unchanged during the whole simulation, and thus, the solution
 100 accuracy of both flow field and water-air interface capture is not degraded for such unsteady problems with large
 101 relative motion. It should be mentioned that the water surface level is kept stationary regardless of the translation or
 102 rotation of the mesh. To achieve this goal, at the beginning the function of α_w needs to be implemented on the boundary
 103 condition where the water volume fraction of each grid cell was assigned according to its global inertial coordinates.
 104 Specifically, the volume fraction is one for the cells located below the interface, and zero for the cells above. The same
 105 treatment of pressure function on the boundary condition also should be defined as a part of the initial condition of
 106 the fluid field. For the air field, the pressure is assumed as constant at the beginning, while the water pressure varies
 107 gradually depending on the depth in the water domain.

2.3. Models and computational setup

The theory governing the vertical water entry of wedges and expressed by equations (4), (5) and (6) is here validated for the case of oblique entry of a symmetric wedge first, mainly focusing on the vertical load characteristic. The oblique water entry has been chosen as the motion of the body resembles that of amphibious aircraft during landing and allows to study the effect of varying both the vertical and horizontal components. In (Russo et al., 2018), the oblique impact of the wedge has been studied by systematically varying the velocity angle α , with the vertical and horizontal motions. The wedge has a width $W = 0.2$ m and a deadrise angle $\beta = 37^\circ$ and it is impacting with the symmetry axis oriented vertically, as seen in Fig. 2. The same configuration is simulated numerically. Besides, in order to carry out a two-dimensional numerical simulation, only 1 cell is set in the y -direction (spanwise direction) with a cell size of 0.002 m. The front and back boundary conditions are defined as symmetry. Fig. 3 shows the details of the mesh topology and the grid density with two zoom-in views in the $x - z$ plane. The length of the square boundary is 10 times the width of the wedge. The computational domain is discretized with structured quadrilateral grids and the minimum size of mesh is 0.0005 m. The right hand and bottom sides were set as velocity inlet, when the boundary condition of pressure outlet was specified on the top and the left sides (see Fig. 3).

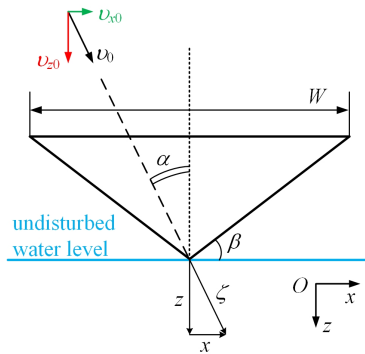


Figure 2: Sketch of the wedge at the onset of the entry along with relevant geometric and dynamic parameters.

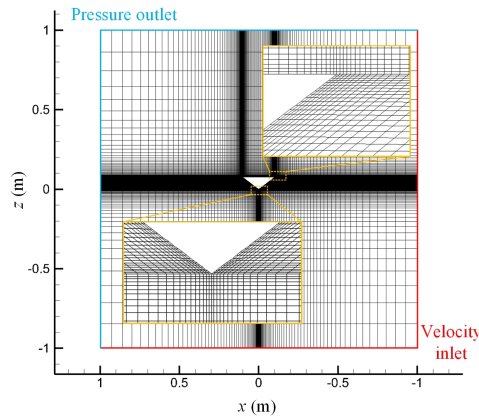


Figure 3: Grid topology and density of the wedge.

As a second step of test, a cabin section, that is a part of the seaplane, is investigated numerically to examine the quantitative relations, referring to Eq. (4), (5) and (6), since the 3D effects affect the slamming force during water impact (Wang et al., 2021b). The geometry parameters of the cabin section are shown in Fig. 4 with length $L = 1.61$ m, width $W = 3.27$ m, deadrise $\beta = 30^\circ$ and mass $M = 600$ kg. The test condition represent that of the experiments in (Chen et al., 2022), where the section is manually lifted to the desired height and released for freely fall. In the simulation, as depicted in Fig. 5, the cabin is initially released near the water surface with different initial impact velocity to study the

128 effect of velocity on the acceleration. Fig. 5 also shows the boundary conditions and the initial relative pressure field
 129 on the left side boundary. A dashed red cuboid was created surrounding the cabin with refined meshes to capture the
 130 water surface more accurately.

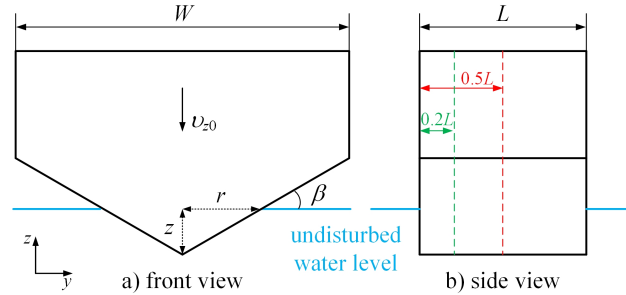


Figure 4: Sketch of the cabin section along with relevant geometric parameters.

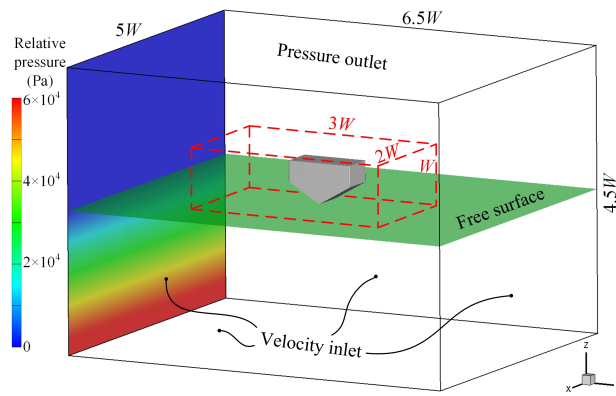


Figure 5: Boundary conditions and the initial flow fields of the cabin section.

131 Eventually, the water landing of V-shaped hull on amphibious aircraft is studied to check the capability of the
 132 theoretical relations (Eq. (4), (5) and (6)) to deal with complex problems and to verify to which extent they are reliable
 133 for engineering applications. A conventional configuration of the fuselage of amphibious aircraft is shown in Fig. 6.
 134 The bottom of hull is divided into two parts, forebody and afterbody, by the step, making it easier to take off on water.
 135 The computational domain was created by a cuboid with size of $6 \times 2 \times 5L$ in length, width and height, respectively (see
 136 Fig. 7), and is regarded large enough for the present study. The whole domain was discretized with Cartesian cells and
 137 prismatic boundary layer grids surrounding the model and moving rigidly without deforming. Three tiers for refining
 138 meshes were assigned to the entire domain as follows: tier 3 for the accurate description of the hydrodynamics about
 139 the hull; tier 2 and tier 1 fan-shaped regions to enable the large range of pitch motion. The cell height in these tiers
 140 is $0.005L$, $0.01L$ and $0.015L$, respectively. The total number of grid cells in the whole domain is almost 12 million.
 141 Note that the wing and tail wing are taken into consideration.

142 3. Results and Discussion

143 3.1. 2D symmetric wedge

144 First, the accuracy and efficiency of the numerical method have been validated for a symmetric wedge. In the
 145 simulation, at $t=0.001$ s, the wedge is dropped freely against calm water from a small distance at 0.002m, entering
 146 the free surface with an initial resultant velocity $v_0 = 2.75$ m/s and velocity angle $\alpha = 20^\circ$ (see Fig. 2). Fig. 8 shows
 147 the comparison between the numerical results of the present study and experimental data (Russo et al., 2018) in terms
 148 of the normalized resultant displacement ζ and acceleration $\ddot{\zeta}$. It can be seen, the results are in good agreement with

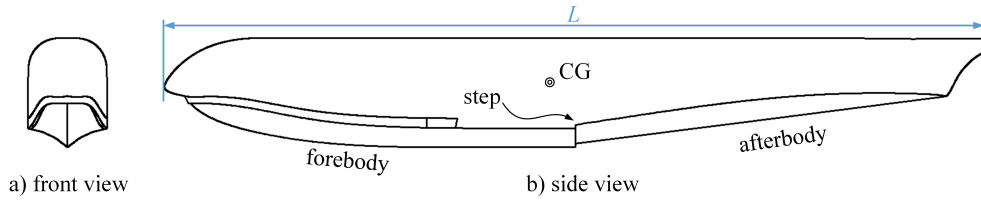


Figure 6: V-shaped hull configuration features of amphibious aircraft.

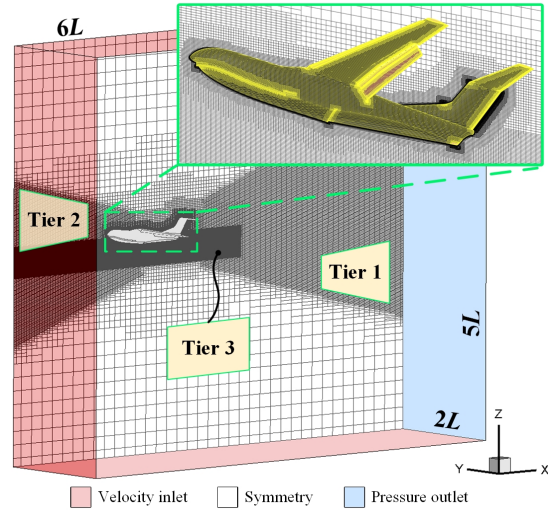


Figure 7: Computational domain and boundary conditions of the amphibious aircraft.

149 experiments, aside from a little discrepancy occurs at the early stage of the acceleration. Theoretically, at the beginning
 150 the acceleration should be close to $-g$, like numerical results show, whereas in the experimental data the acceleration
 151 is immediately positive, probably due to measurement problems in the initial phases (Russo et al., 2018). Also, a good
 152 comparison with another CFD numerical result (Yang and Xu, 2018) can be observed in Fig. 8. Overall, numerical
 153 results exhibit a satisfactory agreement with the experimental data.

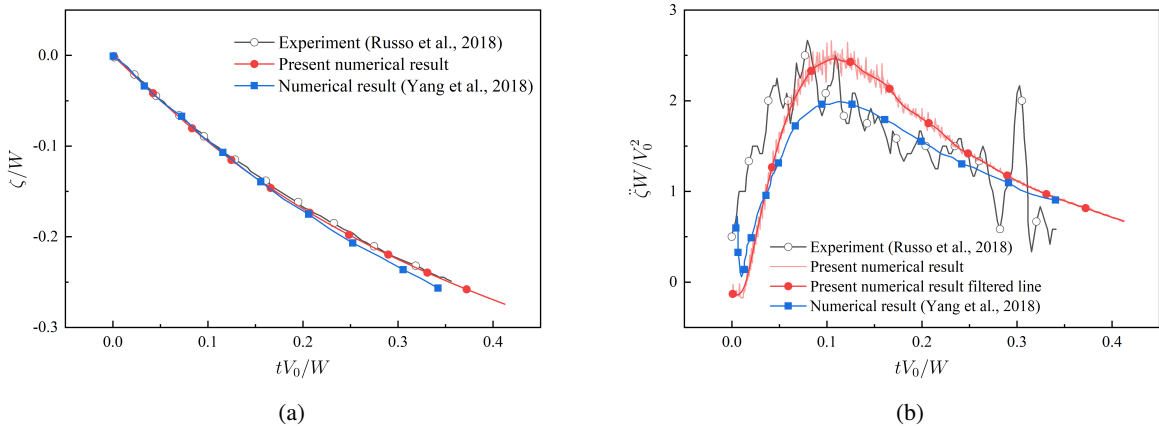


Figure 8: Comparison among the present study, experimental data and numerical results on the oblique water entry of a wedge: (a) normalized resultant displacement; (b) normalized resultant acceleration.

3.1.1. Effect of vertical velocity

Next, in order to better understand the effect of the variation of the vertical velocity, several simulations have been performed for constant v_{x0} and α varying from 10° to 50° , which corresponds to a reduction of the vertical velocity component. The time histories of dimensionless acceleration in z -direction a_z , defined as $a_z = (F_w + F_a - Mg)/Mg$, where F_w and F_a denote the fluid force induced by water and air respectively, are depicted in Fig. 9a, along with several pink crosses marking the maximum value $a_{z\max}$. The data indicate that the increase in α causes a significant reduction of a_z due to the corresponding reduction in the v_{z0} . Note that the positive values of a_z denote upward acceleration. In particular, as v_{z0} drops below a certain value, a_z will experience a smooth trend in proximity to zero, known as 'smooth entry' (Vincent et al., 2018). The data shown in Fig. 9b indicate that $a_{z\max}$ is a linear function of v_{z0}^2 , thus supporting the relationship formulated in the Eq. (4), except for the offset. Furthermore, other series of simulations have been conducted by varying the value of v_{x0} , including the case of zero horizontal velocity. Fig. 10 shows that all the data are aligned on the same straight line, thus confirming the validity of the relationship in the Eq. (4). Note that in the case of $v_{x0}=0.342$ m/s, α varies from 5° to 50° . As highlighted in Table. 1, a linear relation between $a_{z\max}$ and v_{z0}^2 exists, and only minor deviations can be observed in the slope k compared with the theoretical estimate, derived from Eq. (4). However, there is an intercept value of b for the numerical results which is presumably due to the gravity. On the other hand, the data shown in Fig. 10 and Table. 1 display a significant contribution of the vertical component of the velocity to the linear relation, independently of the value of v_{x0} .

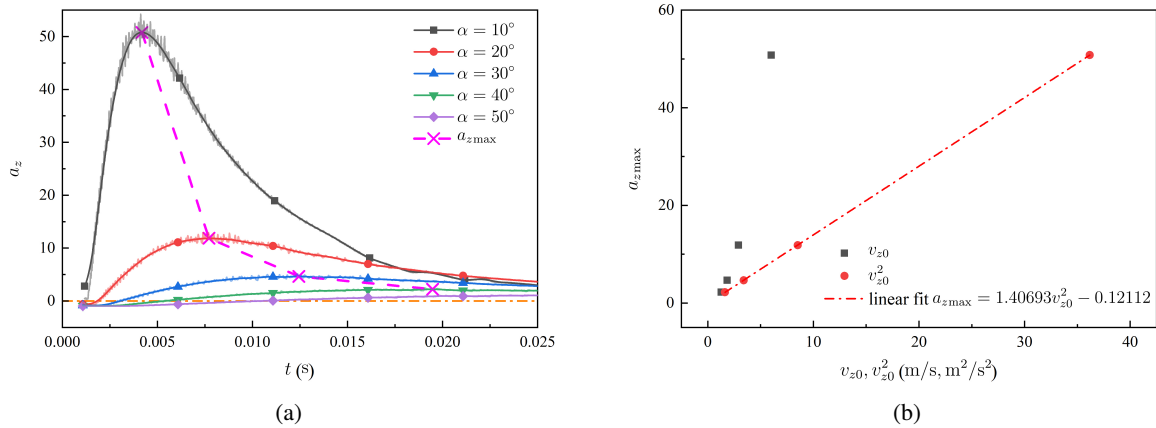


Figure 9: Variation of dimensionless acceleration z with different velocity angle α and fixed horizontal velocity component for oblique water entry: (a) versus time; (b) versus initial vertical velocity.

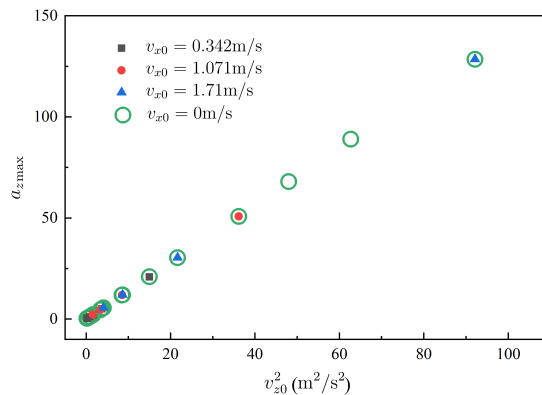


Figure 10: Effect of the horizontal velocity on the relation between $a_{z\max}$ and v_{z0}^2 for oblique water entry.

Table 1

Comparison between theoretical estimate and numerical results for the inclined water entry of a wedge

	$a_{z\max}$			t^*, s			$v_z^*, \text{m/s}$		
	k	err, %	b	k	err, %	b	k	err, %	b
Theoretical value	1.2807	-	-	0.0197	-	-	0.8333	-	-
$v_{x0} = 0.342\text{m/s}$	1.3588	6.09	-0.0509	0.0285	44.67	-0.0046	0.8010	-3.87	0.1121
$v_{x0} = 1.071\text{m/s}$	1.4069	9.85	-0.1211	0.0228	15.73	-0.0014	0.8367	0.41	0.0142
$v_{x0} = 1.710\text{m/s}$	1.3948	8.91	0.0364	0.0185	-6.09	-	0.8308	-0.30	0.0306

171 In Fig. 11, the other four correlated variables are reported, viz., time t^* , penetration depth z^* , velocity v_z^* and the
 172 ratio of velocity κ , defined as $\kappa = v_z^*/v_{z0}$, for the four cases introduced earlier. In Eq. (6), a linear relation between
 173 t^* and reciprocal of the initial vertical velocity v_{z0}^{-1} was established that is similar to the solution in Fig. 11a, despite a
 174 small difference appears on k among the three cases. As listed in Table 1, the error of the numerical values with respect
 175 to the theoretical estimate, varying from 44.67% to -6.09%, shows an obvious decreasing with the growth of v_{x0} . In
 176 fact, when reducing v_{x0} , the corresponding initial vertical velocity for lower α becomes smaller and, consequently,
 177 gravity effects increase causing larger differences with respect to the theoretical formulation which is derived without
 178 considering gravity. In Fig. 11b, the values display a reduction of z^* when increasing v_{z0} , where one can see that the
 179 greater is the v_{z0} , the closer z^* will be to a asymptotic line slightly different from the theoretical result, however, z^*
 180 should be constant in theory as it depends on M and β only (see Eq. (5)). The difference with respect to the theoretical
 181 line depends on the pile-up effect which is not taken into account in Von Karman's momentum conservation and affects
 182 the evaluation of the hydrodynamic behaviour (Mei et al., 1999; Iafrati et al., 2000). Furthermore, the gray shaded area
 183 shows the range at which z^* is close to the constant value and the lowest value of v_{z0} is almost 2.95 m/s in this model,
 184 implying that the theoretical solution is nearly valid only when certain conditions on v_{z0} are met. Fig. 12 shows the
 185 water surface deformation around the wedge at t^* for different cases with a cyan region, where it can be clearly noted
 186 that the displacements of the apex remain almost the same, despite different water jet zones form at the two sides.
 187 In the bottom-right picture, the spray seems to detach from the body and fall down. This is a consequence of the
 188 gravity. Moreover, as shown in all contours, it indicates that the maximum acceleration $a_{z\max}$ occurs before the wedge
 189 is completely submerged.

190 Moving to the relationship between v_z^* and v_{z0} , shown in Fig. 11c and Table 1, a slight difference among the
 191 simulations and theory on k can be observed, the error on k being below 5%. Furthermore, as shown in Fig. 11d, the
 192 trend of κ is similar to the one obtained from z^* , and a gray shaded region can be found where v_z^* is 5/6 times v_{z0}
 193 in agreement with the theoretical estimate. In other words, the value 5/6 about v_z^* and v_{z0} can only be set up when
 194 v_{z0} is greater than 1.85m/s, which is smaller than the limitation 2.95m/s on z^* . As it can be seen in Fig. 9a), the
 195 acceleration experiences two phases, acceleration downwards and then upwards, before reaching the maximum. Since
 196 the wedge, with a deadrise angle $\beta=37^\circ$, undergoes a free fall motion, gravity plays a dominant role at the very early
 197 stage, leading to an accelerating period and an increase in the vertical velocity. Subsequently, with the increase of
 198 hydrodynamic force, the downward acceleration diminishes and gradually turns upwards. Thus, it can be concluded
 199 from Fig. 9a) that, for a given mass of the impacting body, the smaller is the initial vertical velocity, the longer is the
 200 accelerating time. Moreover, four distinctive points exceeding 1.0 are noticeable in Fig. 11d, meaning that the vertical
 201 velocity of the body is larger than initial vertical velocity. Overall, it indicates that the accelerating phase not only
 202 lasts longer, but the effect of the accelerating phase become more dominant than the decelerating phase, as the initial
 203 vertical velocity decreases.

204 It is worth noting that the momentum theorem (Eq. (1)) was obtained without gravity (Mei et al., 1999), whereas the
 205 gravitational field has been added into the numerical simulations. Nevertheless, following the investigation discussed
 206 above, the formulas (4), (5) and (6) derived from Eq. (1) are still available when the initial vertical velocity becomes
 207 larger. In other words, gravity can be neglected with larger velocities, and it has been highlighted in (Zekri et al., 2021).
 208 Whereas, with slow impact speeds, the gravity should be considered in the model (Bertram, 2012), as confirmed by
 209 the discrepancies occurred at the range of low velocities (see Fig. 11b and 11d). Nonetheless, gravity seems to have
 210 no effects on the linear relation between $a_{z\max}$ and v_{z0}^2 , except for the offset. The maximal vertical hydrodynamic force
 211 during impact is then introduced herein, defined as $F_{\text{hd}}^* = M \cdot (a_{\max} \cdot g + g) - F_{\text{hs}}^*$, where F_{hs}^* is the hydrostatic
 212 force approximately calculated by Archimedean principle. Results shown in Fig. 13 indicate that the linear relation

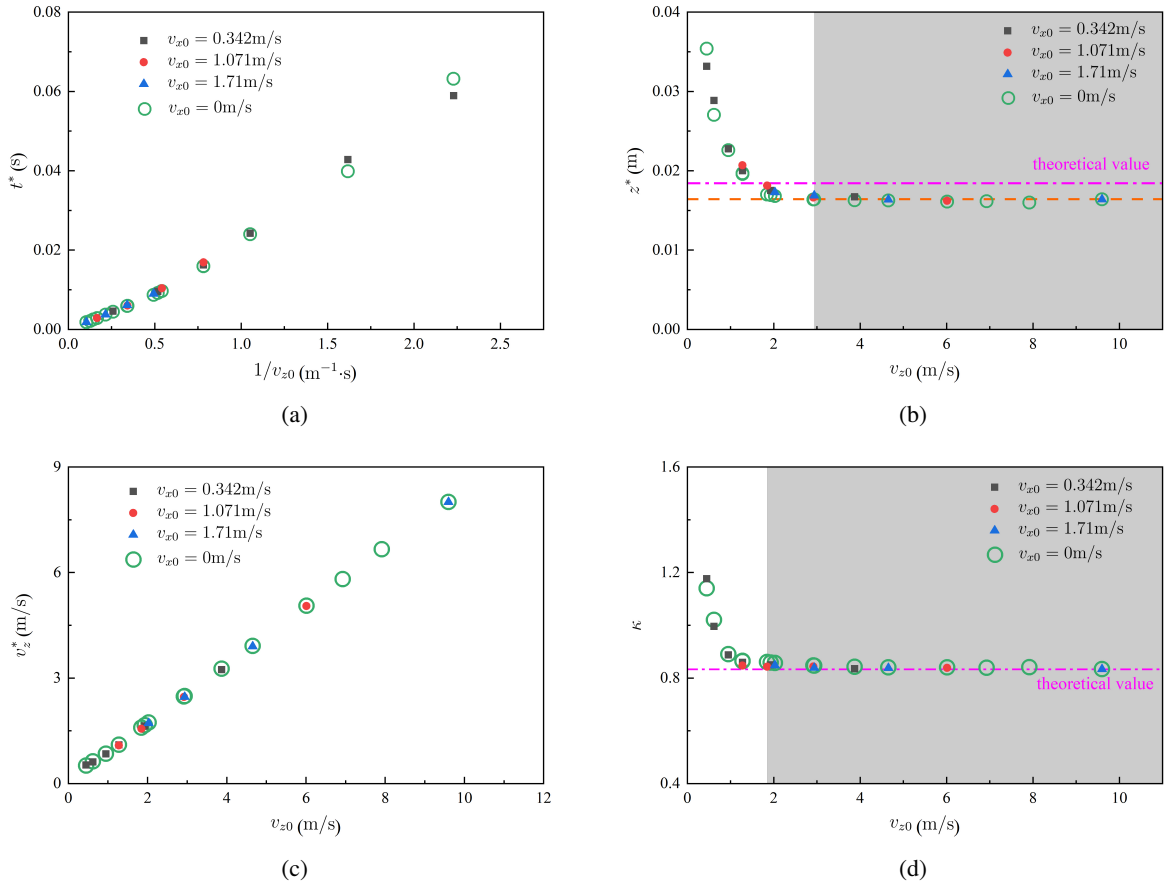


Figure 11: Effect of initial vertical velocity on variable dynamic parameters for the oblique water entry of a wedge: (a) t^* ; (b) z^* ; (c) v_z^* ; (d) κ .

213 still holds which is consistent with (Zekri et al., 2021; Bertram, 2012), who found that ‘*even when gravity is formally*
 214 *of the same order of magnitude as the fluid inertia, the effect of gravity on the hydrodynamic loads is still small and*
 215 *can be approximately neglected*’.

216 Based on the good collapse of the data from different initial horizontal velocity, it is believed that the initial
 217 vertical velocity plays a dominant role on the kinematic characteristics during wedge water entry with the given shape
 218 parameters, indicating that the effect of initial horizontal velocity on the relations can be ignored. For the analytical
 219 solutions based on Eq. (4), (5) and Eq. (6) to be valid, there is a supplementary condition to the momentum theory
 220 which requires that the initial vertical velocity has to higher than a threshold value. Furthermore, the formula for the
 221 added mass, which is usually focused for the vertical water entry, is found to be valid for the oblique entry on the
 222 vertical direction as well.

223 3.1.2. Effect of horizontal velocity

224 In addition to the analysis of the effect of the initial vertical velocity on the load characteristics, for the oblique water
 225 entry of a wedge it is also significant to investigate the role played by the initial horizontal velocity. By assuming v_{z0}
 226 constant and changing α to vary v_{x0} , similar to what done in the previous section, Fig. 14 presents the time histories of
 227 a_x and a_z exerted on the wedge at various velocity angle α , using the fixed vertical velocity component $v_{z0} = 2.943$ m/s,
 228 derived from the previous case of $v_{x0} = 1.071$ m/s and $\alpha = 20^\circ$. As it can be seen, the value of a_x exhibits an obvious
 229 decreasing trend when reducing α upon water impact, whereas no changes are observed in a_z , significantly differing
 230 from the situations of varying initial vertical velocity. Therefore, the data of $a_{x\max}$ are extracted and compared with
 231 three different functions of v_{x0} as illustrated in Fig. 15. It is interesting to note that the data fit well with a linear function,

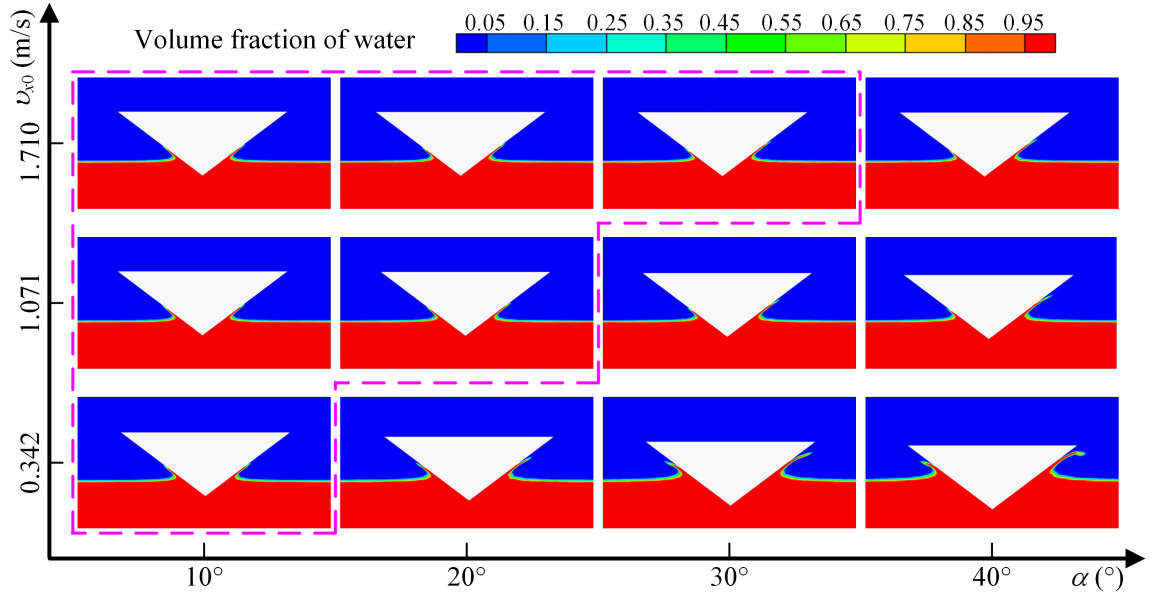


Figure 12: Free surface deformation around the wedge at t^* with different v_{x0} and α .

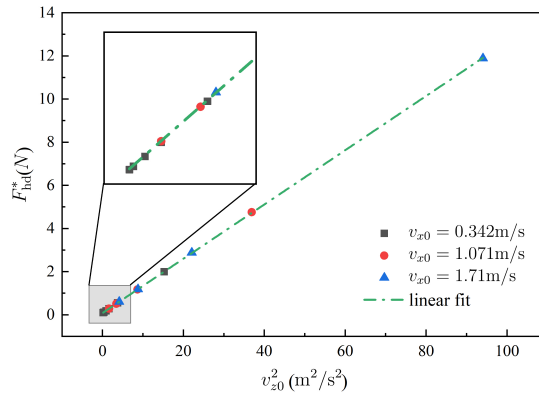


Figure 13: Hydrodynamic forces versus the square of the initial vertical velocity for the oblique water entry of a wedge with different initial velocity.

232 although the function is established between $a_{x\max}$ and v_{x0} , instead of v_{x0}^2 , which is remarkably different from cases of
 233 varying v_{z0} . The pressure contour plots around the wedge with variable α , when $a_{x\max}$ is achieved, are depicted in the
 234 upper side of Fig. 16 and Fig. 17, where the pressure coefficient C_p is defined as $C_p = (p - p_0) / [0.5\rho(v_{z0}^2 + v_{x0}^2)]$, and
 235 the value of v_{x0} is referring to the initial horizontal velocity in the case of $\alpha = 40^\circ$. It can be seen that a higher-pressure
 236 region occurs at the right-hand side of the wedge, whereas a zone with negative pressure is observed on the left, leading
 237 to the variation of a_x . It is therein evidenced that the pressure field varies significantly in the range $\alpha \in [10^\circ, 40^\circ]$, when
 238 a_x reaches the peak value. The comparison between Fig. 16 and Fig. 17 indicates that the water jets originate from
 239 the pressure peak, and the low-pressure zone is close to the apex which is consistent with (Riccardi and Iafrati, 2004;
 240 Judge et al., 2004). Furthermore, flow separation could be expected at the apex which can also lead to cavitation or
 241 ventilation due to horizontal-vertical impact velocity (Judge et al., 2004), provided that fluid dynamic solution method
 242 is able to model cavitation and ventilation phenomena.

243 In order to achieve a better comprehension of the effect of v_{x0} on the impact dynamics, the value of the horizontal
 244 velocity component v_x^* , the ratio of velocity κ_x and time t^* at which a_x reaches its maximal value are provided

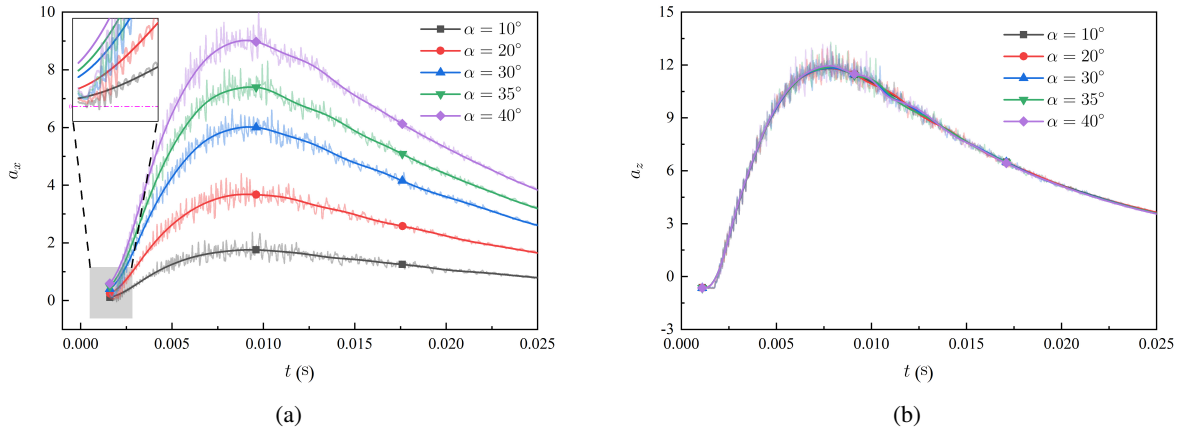


Figure 14: Time histories of dimensionless acceleration in both x - and z -directions with different inclined angles using the fixed vertical velocity component $v_{x0} = 2.943$ m/s: (a) a_x ; (b) a_z .

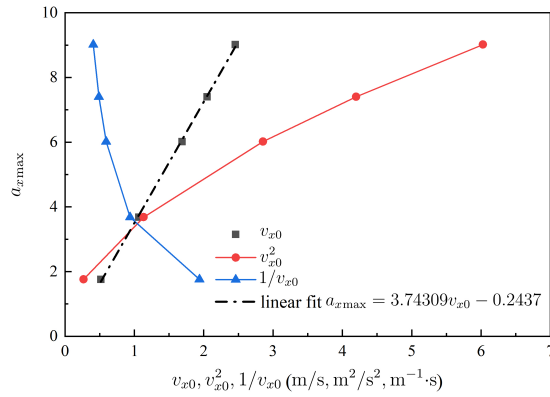


Figure 15: Variation of maximum acceleration x versus initial horizontal velocity.

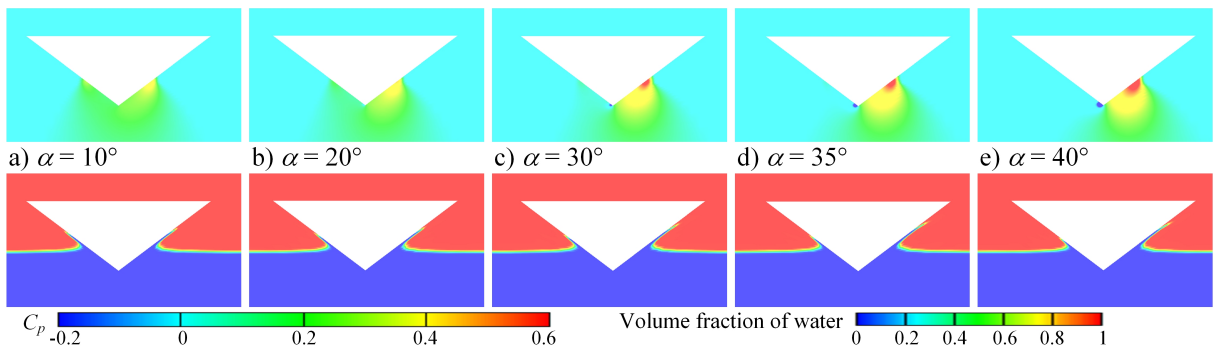


Figure 16: Pressure distribution and water volume fraction for different velocity angle α when a_x reaches its maximum.

245 in Fig. 18. The results are shown for five distinct cases. It's worth noticing that v_x^* varies linearly with v_{x0} , as
 246 $v_x^* = 0.81375v_{x0} + 0.01059$. The parameter k is numerically lower than the analytical one provided by Eq. (5), as
 247 it is shown in Fig. 18b. Nonetheless, the error of k compared to theoretical estimate is -2.35% with a root mean squared
 248 error (RMSE) on κ is 0.0122, thus indicating the theory about $v_z^* - v_{z0}$ derived from vertical entry can be used. Moving

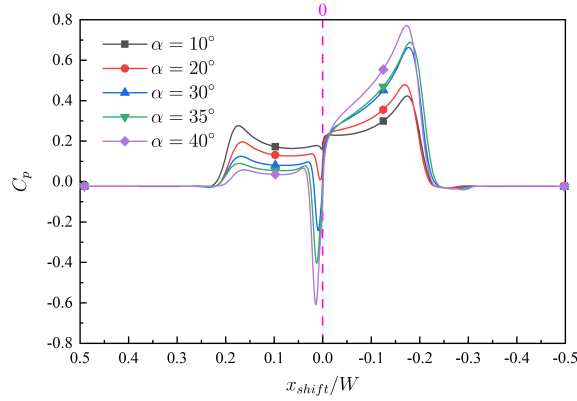


Figure 17: Pressure coefficient along the normalized x -axis for different velocity angle α when a_x reaches its maximum.

249 to Fig. 18c, the trend is quite different from the linear function displayed in Eq. (6) and Fig. 11a for the case of 2D
 250 wedge with various vertical velocities. The numerical values of t^* are almost constant for both cases of v_{x0} and v_{x0}^{-1} ,
 251 and the standard deviation σ of these data is 1.11×10^{-4} . The curves presented in Fig. 18d demonstrate that x^* is
 252 proportional to v_{x0} , expressed as $x^* = 0.00693v_{x0}$, and the results of z^* oscillate slightly around 0.0221 associated
 253 with 2.56×10^{-4} in σ . The above result is confirmed by the lower part of Fig. 16, where no substantial differences
 254 for vertical displacement are observed. In general, linear functions can be found on $a_{x\max} - v_{x0}$ and $v_x^* - v_{x0}$ (see
 255 Fig. 15 and Fig. 18a), except for the relationship between the corresponding time t^* and the initial horizontal velocity
 256 v_{x0} where a constant trend is observed in Fig. 18c.

257 3.2. A cabin section in 3D

258 The above results prove that it is possible to evaluate the load characteristics with the help of the linear relations,
 259 proposed in Eq. (4), (5) and Eq. (6), with large initial vertical velocity. This section presents the results of computational
 260 simulations of the vertical free fall of a cabin section (see Fig. 4), entering the free surface with various initial vertical
 261 velocity v_{z0} . Eleven cases with a series of v_{z0} from 0.5 m/s to 6 m/s are simulated. Fig. 19a shows the evolution of a_z
 262 acting on the cabin during the water entry. It is worth noting that the results have been filtered with a cutoff frequency
 263 62.5 Hz. At the beginning of the impacting, the overall acceleration is negative indicating that gravity dominates and
 264 leads to an increase in the vertical velocity, while the hydrodynamic force only plays an auxiliary role at the onset of
 265 entry. As the body penetrates into the water, a_z turns positive and reaches its peak value subsequently, which means
 266 the hydrodynamic force is dominant. Obviously, a_z is linked with the initial impact velocity. The smaller v_{z0} is, the
 267 smoother the trend of a_z will be, until a point where the peak disappear. Such a behaviour can be also observed in
 268 Fig. 19b, where the pressure coefficient $C_p = (p - p_0)/(0.5\rho v_{z0}^2)$ is computed along the wetted part of the body at
 269 $0.5L$ with v_{z0} chosen as 6 m/s. As the initial impact velocity increases, the overall values of C_p become higher for
 270 selected five cases with different initial vertical velocity, as shown in Fig. 19b, where three extreme values can be
 271 observed. One extreme value is at $y=0$, the apex of the body, so-called stagnation point, where the flow velocity is
 272 almost equal to zero, and the other two extreme values, marked with '+' in Fig. 19b, are inside the grey region. It
 273 can be seen that the distance between the peak points becomes narrower, and the difference is less pronounced as v_{z0}
 274 grows.

275 Fig. 20a demonstrates $a_{z\max}$ is still a linear function to v_{z0}^2 , fitted by $a_{z\max} = 0.1734v_{z0}^2 - 0.1983$, where k is
 276 slightly lower than the theoretical one with -7.57% error, as listed in Table 2. Fig. 20b shows the results of C_p at three
 277 distinctive cross-sections, viz., $0.1L$, $0.2L$ and $0.5L$, for different values of v_{z0} , where the difference δ is caused by
 278 the three dimensional effects and introduces a difference between the numerical and the theoretical solution. The data
 279 show that the value of δ becomes larger as v_{z0} rises, denoting more significant three-dimensional effects.

280 The relations about the other dynamic parameters in 3D cabin section are shown in Fig. 21. As can be seen,
 281 the corresponding time t^* is a linear function of v_{z0}^{-1} in Fig. 21a, although the numerical estimate of the parameter
 282 k is 64.41% different from the theoretical prediction, as also observed in the case of oblique entry of a symmetric
 283 wedge. Looking into the penetration depth z^* , there is a slight difference between the numerical results and the

On applicability of von Karman's momentum theory in predicting the water entry load

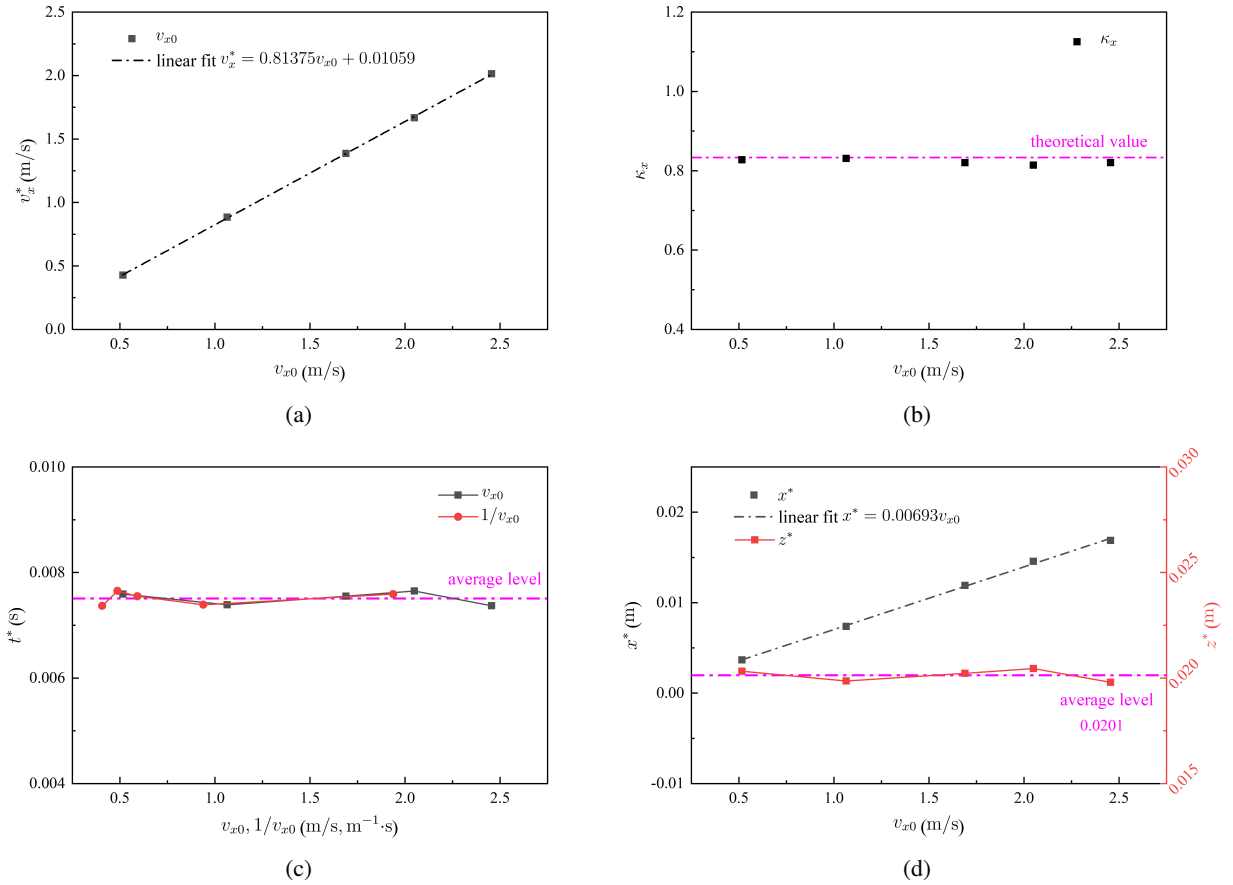


Figure 18: Effect of initial horizontal velocity on variable dynamic parameters: (a) v_x^* ; (b) κ_x ; (c) t^* ; (d) x^* and z^* .

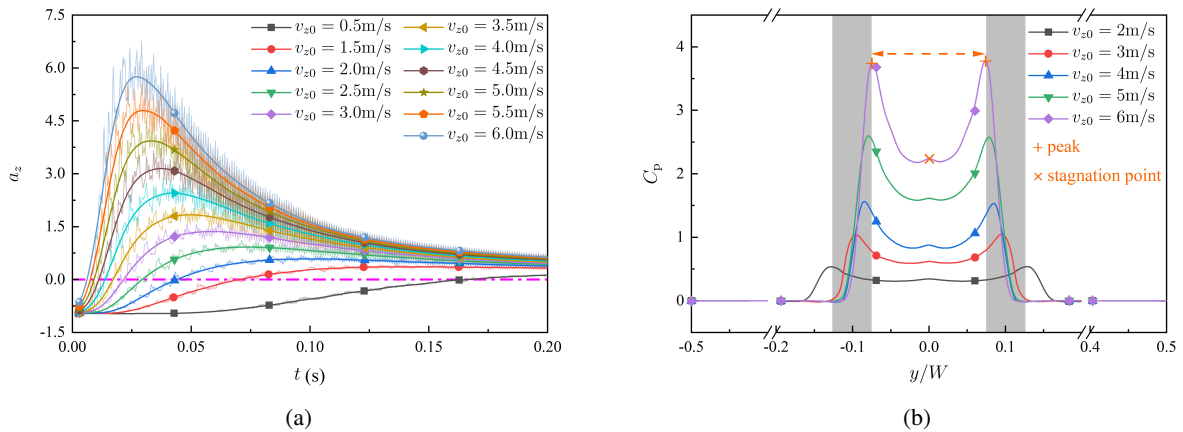


Figure 19: In the case of a 3D cabin section: (a) Time histories of dimensionless acceleration a_z with different initial vertical velocity v_{z0} ; (b) pressure coefficient at $0.5L$ with different v_{z0} .

284 theoretical prediction, however, a new asymptotic line, lying below the theoretical one, appears and all data approach
 285 it asymptotically when increasing v_{z0} . It means that the maximum acceleration of the 3D cabin section occurs at a
 286 smaller depth due to the three-dimensional effects on slamming load (Wang et al., 2021b) and pile-up effects. Another

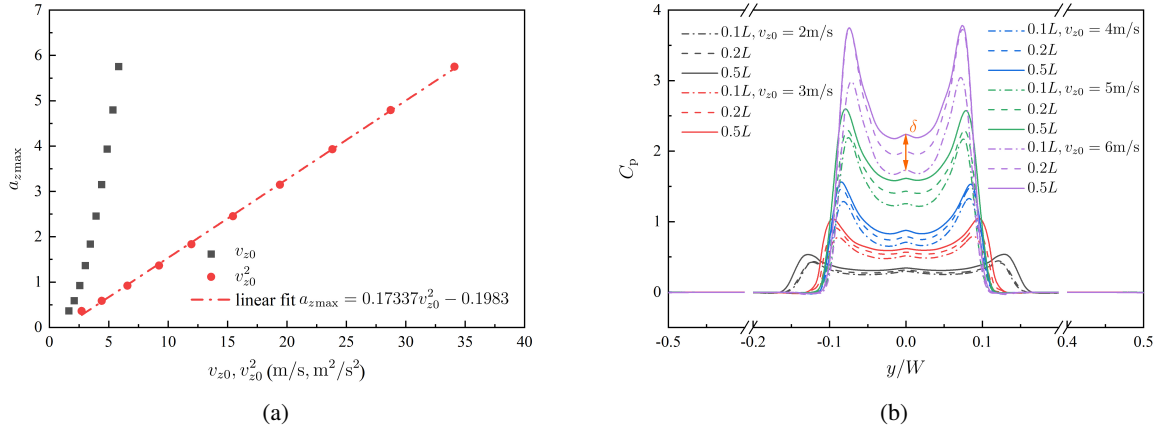


Figure 20: In the case of a 3D cabin section: (a) Variation of $a_{z\max}$ versus v_{z0} and v_{z0}^2 ; (b) pressure coefficient at three distinctive cross-sections for different v_{z0} .

Table 2

Comparison between theoretical estimate and numerical results for cabin section

	$a_{z\max}$			t^*, s			$v_z^*, m/s$		
	k	err, %	b	k	err, %	b	k	err, %	b
Theoretical value	0.1876	-	-	0.1343	-	-	0.8333	-	-
Present study	0.1734	-7.57	-0.1983	0.2208	64.41	-0.0215	0.8135	-2.38	0.2793

287 significant parameter to characterize the impact is the corresponding velocity v_z^* as shown in Fig. 21c, which displays
 288 a linear relation with v_{z0} . Specifically, as seen in Fig. 21d, the value of κ approaches the theoretical line only for v_{z0}
 289 greater than 4.5 m/s, whereas the large difference are observed for smaller initial impact velocities.

290 Subsequently, the instantaneous Froude number (Hulin et al., 2022), $Fr^* = v_z^* / \sqrt{gz^*}$, is introduced here to describe
 291 the combined relations between velocity and penetration depth, when the maximum value of acceleration is reached.
 292 As it can be seen in Fig. 22, Fr^* is found proportional to the initial vertical velocity v_{z0} , in the case of 2D wedge
 293 and 3D cabin section. The proportional relation can also be derived from Eq. (5), where z^* is independent of v_{z0} and
 294 v_z^* is considered as a linear function of v_{z0} . Being $a_{z\max}$ a linear function of v_{z0}^2 , the relationship between maximum
 295 acceleration and the instantaneous Froude number Fr^* can be easily established through Eq. (4), (5), as follows:

$$\frac{a_{z\max}}{(Fr^*)^2} = \frac{a_{z\max} \cdot gz^*}{(v_z^*)^2} = \frac{1}{3} \longrightarrow a_{z\max} = \frac{1}{3} \cdot (Fr^*)^2 \quad (12)$$

296 The detailed results of 2D wedge and 3D cabin section are fitted and summarized in Table 3. It can be seen that the
 297 numerical relations agree well with the theoretical prediction, although in 3D case the value of the slope, k , displays
 298 an obvious deviation associated with the three-dimensional effect. Moreover, Eq. (12) can also be written as:

$$\frac{a_{z\max} \cdot gz^*}{(v_z^*)^2} = \frac{1}{3} \longrightarrow a_{z\max} = \frac{(v_z^*)^2}{3g \cdot z^*} \quad (13)$$

299 providing a strong coupled relation among $a_{z\max}$, v_z^* and z^* , instead of three separate expressions (see Eq. (4) and (5)
 300).

301 3.3. V-shaped hull on amphibious aircraft

302 Herein, the quantitative relations discussed above, (Eq. (4), (5) and (6)), are employed to examine the effect of
 303 initial vertical velocity v_{z0} on the load characteristics for the water landing of the V-shaped hull on amphibious aircraft

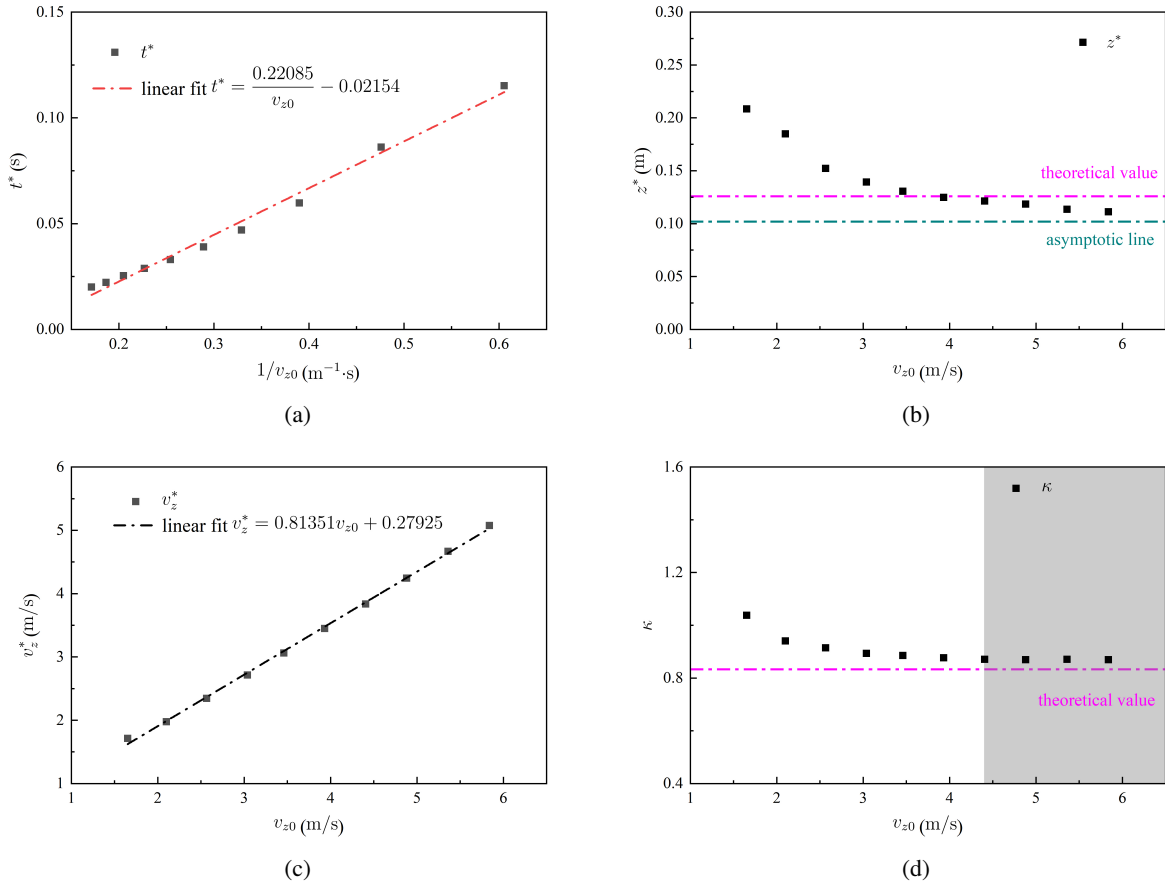


Figure 21: Effect of the initial vertical velocity on the different parameters for the case of a 3D cabin section: (a) t^* ; (b) z^* ; (c) v_z^* ; (d) κ .

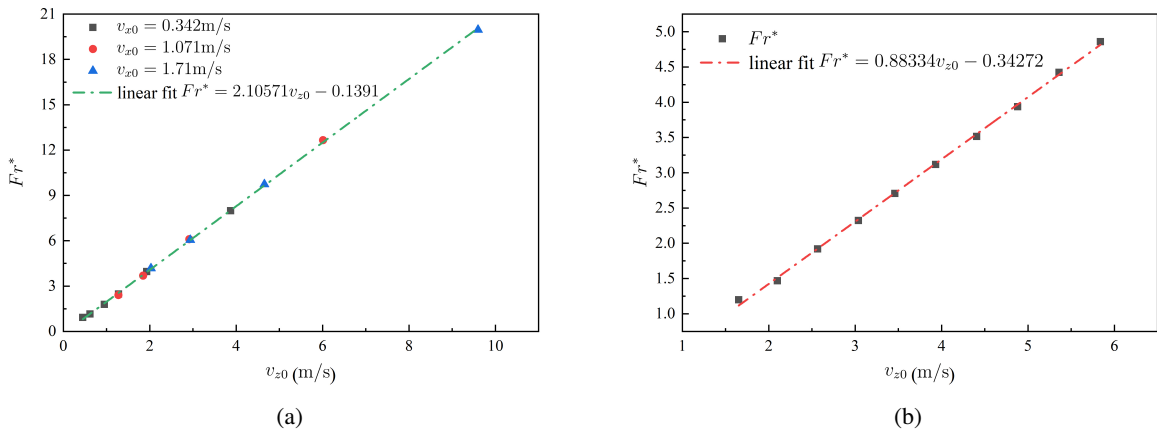


Figure 22: The instantaneous Froude number as a linear function of the initial velocity: (a) 2D wedge; (b) 3D cabin section.

304 (see Fig. 6). A set of numerical simulations is carried out with constant horizontal flight velocity $v_{x0} = 37$ m/s, which is
 305 determined as $v_{x0} = 0.94\sqrt{2G/\rho SC_L}$, where G is the weight of aircraft, S wing area and C_L lift coefficient regarding
 306 to the landing scenario (Lu et al., 2021). The initial pitch θ_0 is set as 7° which is considered as the suitable angle for

Table 3

 Function of $a_{z\max}$ and Fr^* derived from theoretical estimate and numerical results for a 2D wedge and a 3D cabin section.

	Expression	Error of k , %
Theoretical estimation	$a_{z\max} = \frac{1}{3} \cdot (Fr^*)^2$	-
2D wedge	$a_{z\max} = 0.32142 \cdot (Fr^*)^2 + 0.009169$	-3.57
3D cabin section	$a_{z\max} = 0.24417 \cdot (Fr^*)^2 - 0.05474$	-26.75

307 landing event in the previous study (Lu et al., 2021). Both the fixed and free pitch conditions have been simulated in
 308 the present study. Note that the wing components are taken into consideration in the present study.

309 Results, shown in Fig. 23, indicate that a_z decrease when reducing v_{z0} in both conditions. It is worth noting that
 310 as v_{z0} decreases below 1.5 m/s, the overall trend and the amplitudes of a_z in each condition are quite similar, aside
 311 from the time lags. Differently from the conventional impact problem, the amphibian has aerodynamic devices, such
 312 as wings and tail wings, which introduce additional force components affecting the aircraft dynamics. Fig. 24 shows
 313 the parameter c_{aero} , which is the ratio between aerodynamic force to fluid force in the vertical direction derived for the
 314 different cases, when a_z reaches the highest amplitude during the landing motion. It is shown that the parameter c_{aero}
 315 is always below 40% and diminishes when increasing v_{z0} , thus indicating that the hydrodynamic force acting on the
 316 fuselage becomes larger as v_{z0} grows, as expected.

317 Fig. 25 illustrates the pressure distribution at the bottom of the aircraft when a_z reaches its peak. The main fuselage
 318 portion striking with the free surface is the region over the forebody near the step. Note that the pressure coefficient
 319 displayed in the graph is defined as $C_p = (p - p_0)/(0.5\rho v_{x0}^2)$, where v_{z0} is neglected being $v_{x0} = 37$ m/s much greater
 320 than v_{z0} . The pressure peaks occur at the chine flare, after which the hydrodynamic decreases with the formation of
 321 a triangle-shaped region of positive pressure near the step. Correspondingly, negative pressure areas occur behind the
 322 step and the stern of the fuselage. The occurrence of negative pressures at the back of the fuselage is a consequence of
 323 the longitudinal curvature and it can be easily explained by exploiting a 2D+t concept in which the local cross section
 324 undergoes a water exit phase (Del Buono et al., 2021). The data also indicate that the high-pressure regions become
 325 smaller in size and reduce in magnitude when decreasing v_{z0} , which is coherent with the overall downtrend on the
 326 evolutions of a_z revealed in Fig. 23.

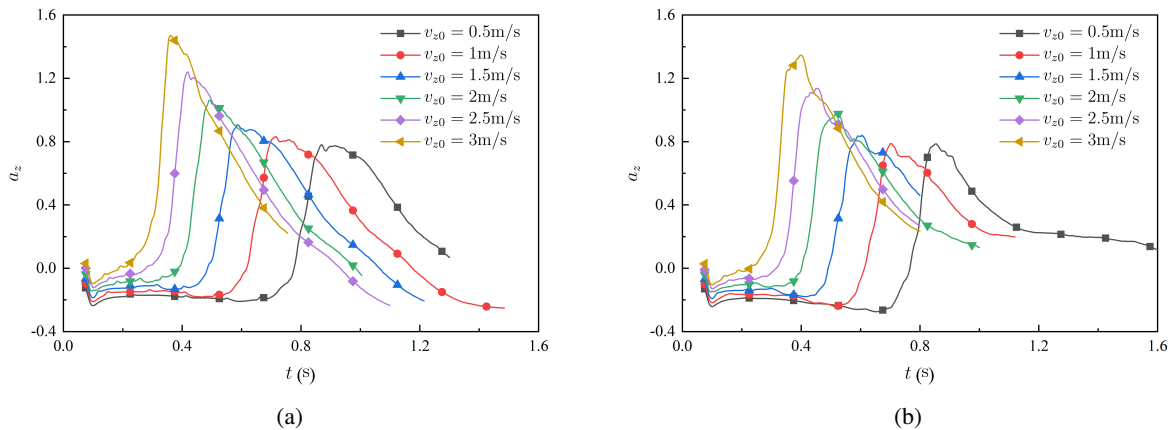


Figure 23: Comparison of fixed and free pitching condition on dimensionless acceleration in z -direction with different initial vertical velocity for the amphibious aircraft: (a) fixed pitch; (b) free pitch.

327 In order to achieve a better comprehension of the effect of the impact velocity on accelerations, the maximal values
 328 of a_z are drawn as a function of the square of vertical velocity v_{z0}^2 in Fig. 26, although it is difficult to derive the slope
 329 k from theoretical estimate Eq. (4). In the presence of a high horizontal speed, the pressure doesn't depend much on
 330 the vertical velocity but rather on the horizontal velocity, pitch angle and pitch dynamics. Furthermore, there are the

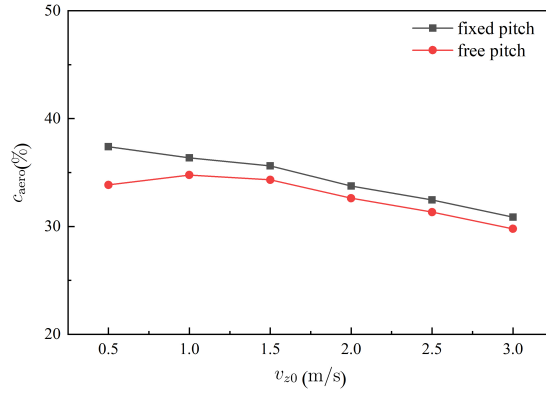


Figure 24: Ratio of the aerodynamic to the fluid force as a function of v_{z0} .

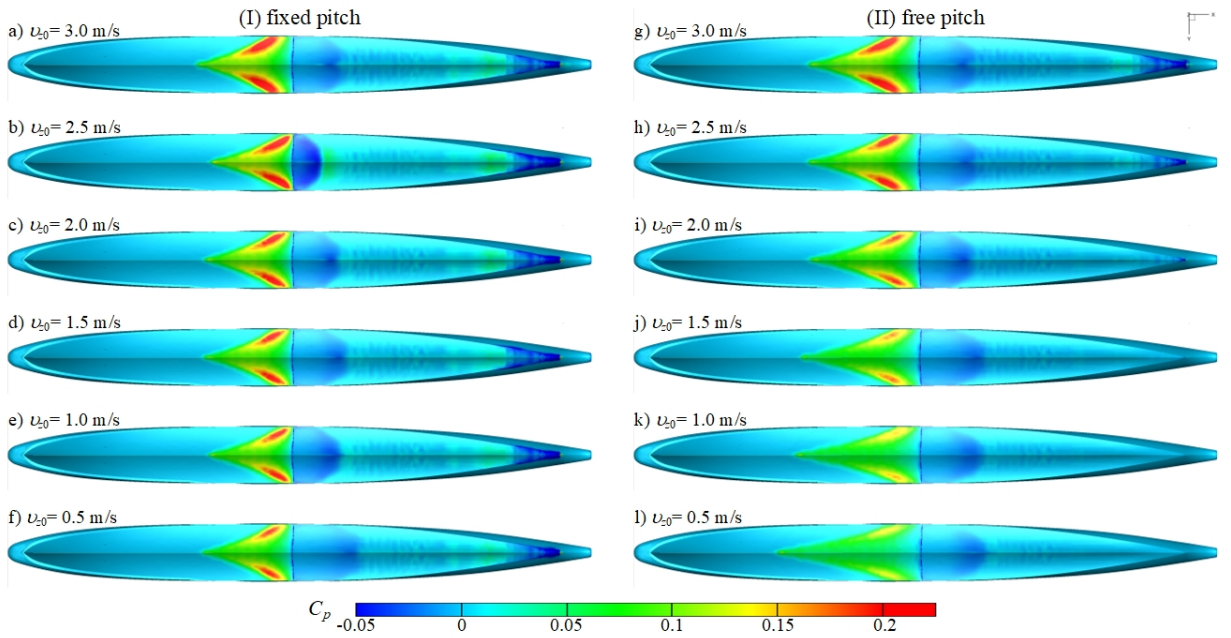


Figure 25: Pressure distribution at the bottom of the aircraft for different v_{z0} at t^* .

331 effects associated with the suction and the double-stepped planing phenomenon which are not accounted for in the
 332 theoretical model (see Fig. 27). Instead, the linearity on $a_{zmax} - v_{z0}^2$ can be found as well, despite a little deviation
 333 appears when v_{z0} is below 1m/s on the fixed pitching situation. The results of a_{zmax} with fixed pitch is above that with
 334 free pitch. For instance, the high-pressure region presented in Fig. 25c) is larger than that in Fig. 25i).

335 Owing to a considerable change on estimate of $a_{zmax} - v_{z0}^2$, it is necessary to check the effectiveness on Eq. (5) and
 336 (6). Fig. 28 shows the variation of other four gauged factors by changing the initial impacting velocity v_{z0} , when the
 337 acceleration reaches its peak. As it can be seen in Fig. 28a, the larger the vertical velocity is, the shorter the time interval
 338 is, implying that the load distribution in time is smoother for lower v_{z0} . Moreover, there is no proportionality between
 339 $t^* - v_{z0}^{-1}$ in both cases of fixed and free pitch. Moving to penetration depth z^* Fig. 28b, a quite different evolution
 340 emerges between the fixed and free pitch conditions. In the fixed pitch condition small variations about the mean value
 341 occur, whereas, in the free pitch condition the depth z^* grows as v_{z0} increases gradually and approaching an asymptotic
 342 value. It is worth noticing that there is an inverse trend compared to the cases of wedge and cabin section. The depth,
 343 z^* , exhibits much smaller variations when an attitude control mode (fixed pitch) is exerted on the aircraft.

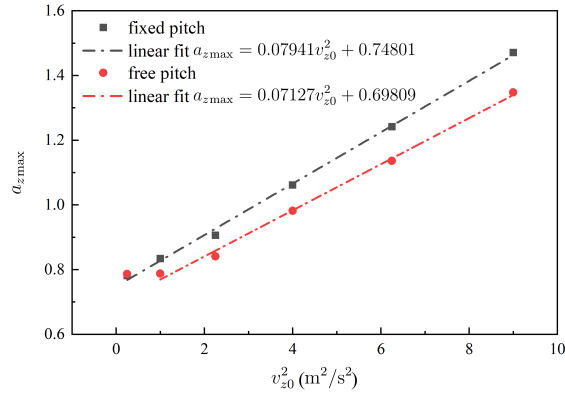


Figure 26: Effect of the pitch motion, fixed and free, on the relation between $a_{z\max}$ and v_{z0}^2 .

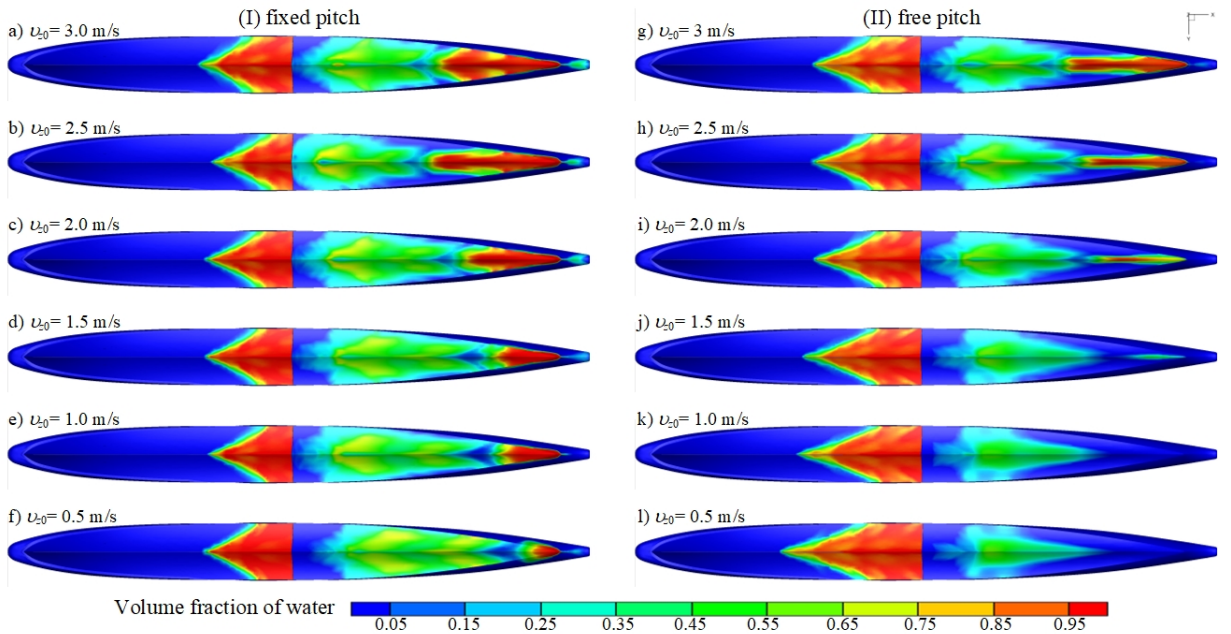


Figure 27: Water volume fraction at the bottom of the aircraft for different v_{z0} at t^* .

344 The results of maximal draught z_{\max} , reached by the hull, are also depicted in Fig. 28b. Of course, z_{\max} is above
 345 z^* , meaning that while a_z attains its maximum, the aircraft continues to move downwards. It shows a monotonous
 346 increasing trend on the function of z_{\max} to v_{z0} for the case of fixed pitch, while a valley occurs in the free pitch motion.
 347 Turning to the behavior of the corresponding velocity v_z^* , it is interesting to see that the two cases share a quite similar
 348 evolution in $v_z^* - v_{z0}$, as presented in Fig. 28c and 28d. Specifically, there is a turning point where v_{z0} equals 1.5 m/s,
 349 whereas the trend is similar afterwards. On the left side of turning point, the results of fixed pitch are lower than that of
 350 free pitch. The blue dashed rectangle indicates the range at which v_z^* is above v_{z0} , in other words, $\kappa > 1$ (see Fig. 28d),
 351 meaning that gravity plays a significant role when v_{z0} is smaller than a certain value as mentioned on Sec. 3.1.1. It
 352 can be seen that the relation of $v_z^* - v_{z0}$ is not linear, quite different from the theoretical trend. Whereas, in Fig. 28d, it
 353 is worth noting that all data approach the theoretical estimate, $5/6$, which means κ is still valid to some extent. Thus,
 354 the relations derived from Eq. (4) and Eq. (5) are partly useful for the tendency prediction on $a_{z\max}$ and κ through a
 355 simple analysis.

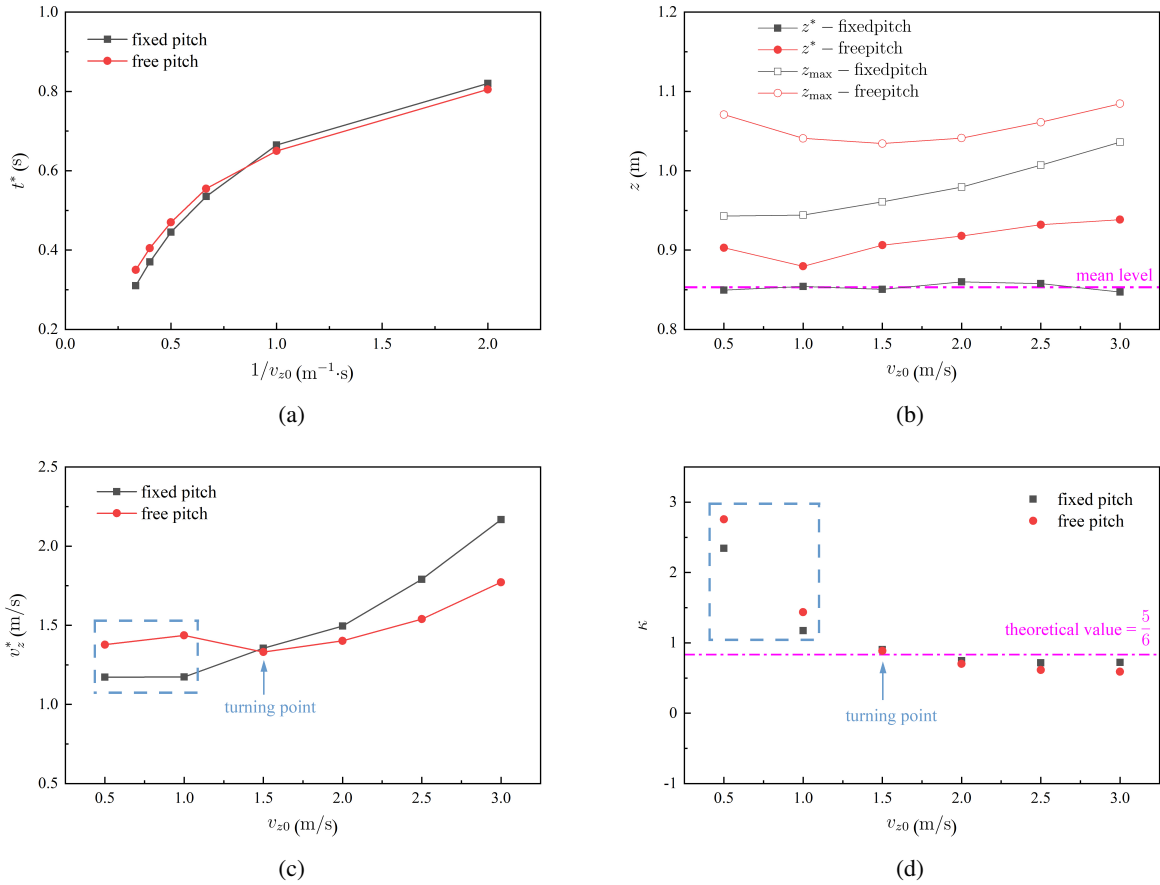


Figure 28: Effect of initial vertical velocity on variable dynamic parameters for the case of the amphibious aircraft: (a) t^* ; (b) z^* ; (c) v_z^* ; (d) κ .

Table 4

Summary of theoretical quantitative relations compared with simulated results among three cases: simulated trend (black solid line); theoretical estimate (red dashed line); simulated asymptotic value (magenta dashed line)

terms	theoretical relations	2D symmetric wedge		3D cabin section		amphibious aircraft	
		fixed pitch	free pitch	fixed pitch	free pitch	fixed pitch	free pitch
$a_{zmax} - v_{z0}^2$	linear	✓	-	✓	-	✓	-
$t^* - v_{z0}^{-1}$	linear	✓	-	✓	-	×	-
$z^* - v_{z0}$	constant	×	-	×	-	constant	×
$v_z^* - v_{z0}$	linear	✓	-	✓	-	×	-
$\kappa - v_{z0}$	constant, 5/6	×	-	×	-	×	-

356 4. Conclusion

357 In the present study, the load characteristics of three models, such as a 2D symmetric wedge water entry, a 3D
 358 cabin section water entry and an amphibious aircraft landing on water have been investigated numerically. The effect
 359 of initial vertical velocity on the maximum acceleration, together with several relationships based on the transformation

of momentum theorem, have been thoroughly analyzed. Contributions and findings are summarized in Table 4, which can be described as:

1) For the three V-shaped sectional area of bodies, such as 2D wedge, 3D cabin section and amphibious aircraft, impacting on water surface, the maximum vertical acceleration increases with the initial vertical velocity, and it is found herein that the value of maximal vertical acceleration is proportional to the square of the initial vertical impacting velocity. For oblique entry, the effect of horizontal velocity on acceleration has also been investigated and it is observed that the maximum horizontal acceleration is a linear function of initial horizontal velocity, rather than its square value.

2) Another significant parameter, that these three models share the same trend, is the ratio of the corresponding velocity to the initial velocity, κ . Following the theoretical formulation, the value should be constant, 5/6, while the numerical results approach it in the case of large initial vertical velocity. It indicates that a threshold value of initial vertical velocity needs to be emphasized to make the theoretical result available. In other words, gravity can be neglected with larger velocities, however, with slow impact speeds, gravity should be considered in the model.

3) For the relationship between penetration depth and the initial vertical velocity, the simulated results approach an asymptotic line (different from the theoretical estimate) with the increase of velocity in the 2D wedge case and the cabin section case. The difference between the numerical asymptotic line and the theoretical estimate is mainly caused by the water pile-up effect. For the 3D cabin section, the three-dimensional water flow in the spanwise direction could also be responsible for the difference. Considering the complicated geometry of the hull, it is hard to determine the theoretical estimate. The numerical results of fixed pitch present a constant trend, whereas a constant value is not reached in the case of free pitch.

4) Looking into other two linear relations, $t^* - v_{z0}^{-1}$ and $v_z^* - v_{z0}$, shown in Table 4, they can be established upon the wedge and the cabin section compared with the theoretical results, while it is invalid for the hull. Besides, in the case of 2D wedge and 3D cabin section, the instantaneous Froude number, Fr^* , is displayed to describe the combined relations between velocity and penetration depth, when the maximum value of acceleration is satisfied. Due to the relationship of $Fr^* - v_{z0}$ and $a_{z\max} - v_{z0}^*$, the maximum acceleration $a_{z\max}$ is one third of the square of the instantaneous Froude number Fr^* . Moreover, a strong coupled relation among $a_{z\max}$, v_z^* and z^* is found, $a_{z\max} = (v_z^*)^2 / (3g \cdot z^*)$.

A. Appendix

In order to obtain the instantaneous acceleration shown in Eq. (3), time derivative of the instantaneous velocity can be analytically computed as:

$$\begin{aligned}
 a(t) &= \dot{v}(t) = \frac{d}{dt} \left(\frac{2M \tan^2(\beta) v_0}{2M \tan^2(\beta) + \pi \rho z^2(t)} \right) \\
 &= 2M \tan^2(\beta) v_0 \cdot \frac{d}{dt} \left(\frac{1}{2M \tan^2(\beta) + \pi \rho z^2(t)} \right) \\
 &= 2M \tan^2(\beta) v_0 \cdot \left(-\frac{1}{(2M \tan^2(\beta) + \pi \rho z^2(t))^2} \right) \cdot 2\pi \rho \cdot z(t) \cdot \dot{z}(t) \\
 &= -\frac{(2M \tan^2(\beta) v_0)^2}{(2M \tan^2(\beta) + \pi \rho z^2(t))^2} \cdot \frac{2\pi \rho \cdot z(t) \cdot \dot{z}(t)}{2M \tan^2(\beta) v_0} \\
 &= -v^2(t) \cdot \frac{2\pi \rho \cdot z(t) \cdot \dot{z}(t)}{2M \tan^2(\beta) v_0} \\
 &= -\frac{\pi \rho z(t)}{M v_0 \tan^2(\beta)} \cdot v^3(t)
 \end{aligned} \tag{A1}$$

The minus sign indicates that the direction of acceleration is opposite to the direction of velocity. Besides, we define that the positive value of acceleration is upwards, while the velocity and the penetration depth are positive downwards.

388 The acceleration reaches its peak value when $\dot{a}(t) = 0$, that is,

$$\begin{aligned}\dot{a}(t) &= \frac{d}{dt} \left(-\frac{\pi\rho \cdot z(t)}{Mv_0 \tan^2(\beta)} \cdot v^3(t) \right) \\ &= -\frac{\pi\rho}{Mv_0 \tan^2(\beta)} \cdot \frac{d}{dt} (z(t) \cdot v^3(t)) = 0\end{aligned}\quad (\text{A2})$$

389 Dividing out the constant term, Eq. (A2) can be rewritten as:

$$\frac{d}{dt} (z(t) \cdot v^3(t)) = v^4(t) + z(t) \cdot 3v^2(t) \cdot a(t) = 0 \longrightarrow v^2(t) + 3z(t) \cdot a(t) = 0 \quad (\text{A3})$$

390 Substituting Eq. (A1) into the second term of this last equation, the Eq. (A3) can be expressed as:

$$v^2(t) - \frac{3\pi\rho \cdot z^2(t)v^3(t)}{Mv_0 \tan^2(\beta)} = 0 \longrightarrow 1 - \frac{3\pi\rho \cdot z^2(t)v(t)}{Mv_0 \tan^2(\beta)} = 0 \quad (\text{A4})$$

391 Then, a new expression of the instantaneous velocity can be obtained as:

$$v(t) = \frac{Mv_0 \tan^2(\beta)}{3\pi\rho \cdot z^2(t)} \quad (\text{A5})$$

392 Besides, the expression of the instantaneous velocity is also given by Eq. (2). Then, using Eq. (2) and (A5), we obtain
393 the corresponding penetration depth z^* :

$$\frac{2M \tan^2(\beta)v_0}{2M \tan^2(\beta) + \pi\rho z^2(t)} = \frac{Mv_0 \tan^2(\beta)}{3\pi\rho \cdot z^2(t)} \quad (\text{A6})$$

$$z(t) = \sqrt{\frac{2M}{5\pi\rho}} \tan(\beta) = z^* \quad (\text{A7})$$

394 Substituting Eq. (A7) into Eq. (A5), the corresponding velocity v^* can be expressed as:

$$v = \frac{Mv_0 \tan^2(\beta)}{3\pi\rho \cdot \frac{2M \tan^2(\beta)}{5\pi\rho}} = \frac{5}{6}v_0 \quad (\text{A8})$$

395 Finally, by combing Eqs. (A1), (A7) and (A8), the maximal acceleration in the positive direction can be obtained
396 as:

$$\begin{aligned}a^* &= \frac{\pi\rho \cdot z^*}{Mv_0 \tan^2(\beta)} \cdot (v^*(t))^3 \\ &= \frac{\pi\rho}{Mv_0 \tan^2(\beta)} \cdot \sqrt{\frac{2M}{5\pi\rho}} \tan(\beta) \cdot \left(\frac{5v_0}{6}\right)^3 \\ &= v_0^2 \left(\frac{5}{6}\right)^3 \frac{1}{\tan(\beta)} \sqrt{\frac{2\pi\rho}{5M}}\end{aligned}\quad (\text{A9})$$

397 Acknowledgments

398 This work has been supported by China Scholarship Council (CSC, No. 202106830092) and the Project TORPEDO
 399 (inTerazione fluidO stRuttura in ProblEmi Di impattO) cooperated in the Institute of Marine Engineering of the
 400 National Research Council of Italy. The supports from Open Foundations of EDL Laboratory (EDL19092111) and
 401 the Aeronautical Science Foundation of China under grant no. 20182352015 are also acknowledged.

402 CRedit authorship contribution statement

403 **Yujin Lu:** Conceptualization, Methodology, Software, Investigation, Data Curation, Visualization, Writing - Orig-
 404 inal Draft. **Alessandro Del Buono:** Validation, Investigation, Formal analysis, Writing - Review & Editing. **Tianhang**
 405 **Xiao:** Conceptualization, Writing - Review & Editing, Supervision. **Alessandro Iafrati:** Project administration,
 406 Writing - Review & Editing, Supervision. **Shuanghou Deng:** Funding acquisition, Writing - Review & Editing,
 407 Supervision. **Jinfa Xu:** Resources, Supervision.

408 References

- 409 Abraham, J., Gorman, J., Reseghetti, F., Sparrow, E., Stark, J., Shepard, T., 2014. Modeling and numerical simulation of the forces acting on a
 410 sphere during early-water entry. *Ocean Engineering* 76, 1–9. doi:10.1016/j.oceaneng.2013.11.015.
- 411 Benson, J.M., Bidwell, J.M., 1945. Bibliography and Review of Information Relating to the Hydrodynamics of Seaplanes. Technical Report NACA
 412 ACR-L5G28. NACA. Washington, D. C.
- 413 Bertram, V., 2012. Practical Ship Hydrodynamics. 2 ed.. Butterworth-Heinemann, Kidlington. chapter 4. pp. 138–145. doi:10.1016/
 414 C2010-0-68326-X.
- 415 Bisagni, C., Pigazzini, M.S., 2017. Modelling strategies for numerical simulation of aircraft ditching. *International Journal of Crashworthiness* 23,
 416 377–394. doi:10.1080/13588265.2017.1328957.
- 417 Breton, T., Tassin, A., Jacques, N., 2020. Experimental investigation of the water entry and/or exit of axisymmetric bodies. *Journal of Fluid*
 418 *Mechanics* 901, A37. doi:10.1017/jfm.2020.559.
- 419 Chen, J., Xiao, T., Wu, B., Wang, F., Tong, M., 2022. Numerical study of wave effect on water entry of a three-dimensional symmetric wedge.
 420 *Ocean Engineering* 250, 110800. doi:10.1016/j.oceaneng.2022.110800.
- 421 Del Buono, A., Bernardini, G., Tassin, A., Iafrati, A., 2021. Water entry and exit of 2d and axisymmetric bodies. *Journal of Fluids and Structures*
 422 103, 103269. doi:10.1007/s13272-017-0257-0.
- 423 Duan, X., Sun, W., Chen, C., Wei, M., Yang, Y., 2019. Numerical investigation of the porpoising motion of a seaplane planing on water with high
 424 speeds. *Aerospace Science and Technology* 84, 980–994. doi:10.1016/j.ast.2018.11.037.
- 425 Gong, K., Liu, H., Wang, B., 2009. Water entry of a wedge based on sph model with an improved boundary treatment. *Journal of Hydrodynamics*
 426 21, 750–757. doi:10.1016/S1001-6058(08)60209-7.
- 427 Guo, B., Liu, P., Qu, Q., Wang, J., 2013. Effect of pitch angle on initial stage of a transport airplane ditching. *Chinese Journal of Aeronautics* 26,
 428 17–26. doi:10.1016/j.cja.2012.12.024.
- 429 Hirt, C.W., Nichols, B.D., 1981. Volume of fluid (vof) method for the dynamics of free boundaries. *Journal of Computational Physics* 39, 201–225.
 430 doi:10.1016/0021-9991(81)90145-5.
- 431 Hughes, K., Vignjevic, R., Campbell, J., Vuyst, T.D., Djordjevic, N., Papagiannis, L., 2013. From aerospace to offshore: Bridging the numerical
 432 simulation gaps-simulation advancements for fluid structure interaction problems. *International Journal of Impact Engineering* 61, 48–63.
 433 doi:10.1016/j.ijimpeng.2013.05.001.
- 434 Hulin, F., Del Buono, A., Tassin, A., Bernardini, G., Iafrati, A., 2022. Gravity effects in two-dimensional and axisymmetric water impact models.
 435 *Journal of Fluid Mechanics* 944, A9. doi:10.1017/jfm.2022.448.
- 436 Iafrati, A., 2016. Experimental investigation of the water entry of a rectangular plate at high horizontal velocity. *Journal of Fluid Mechanics* 799,
 437 637–672. doi:10.1017/jfm.2016.374.
- 438 Iafrati, A., Carcaterra, A., Ciappi, E., Campana, E.F., 2000. Hydroelastic analysis of a simple oscillator impacting the free surface. *Journal of Ship*
 439 *Research* 44, 278–289. doi:10.5957/jsr.2000.44.4.278.
- 440 Iafrati, A., Grizzi, S., 2019. Cavitation and ventilation modalities during ditching. *Physics of Fluids* 31, 052101. doi:10.1063/1.5092559.
- 441 Judge, C., Troesch, A., Perlin, M., 2004. Initial water impact of a wedge at vertical and oblique angles. *Journal of Engineering Mathematics* 48,
 442 279–303. doi:10.1023/B:engi.0000018187.33001.e1.
- 443 von Karman, T., 1929. The Impact on Seaplane Floats During Landing. Technical Report NACA TN-321. NACA. Washington, D. C.
- 444 Korobkin, A., 2004. Analytical models of water impact. *European Journal of Applied Mathematics* 15, 821–838. doi:10.1017/
 445 S0956792504005765.
- 446 Korobkin, A.A., Scolan, Y.M., 2006. Three-dimensional theory of water impact. part 2. linearized wagner problem. *Journal of Fluid Mechanics*
 447 549, 343–373. doi:10.1017/S0022112005008049.
- 448 Lu, Y., Xiao, T., Deng, S., Zhi, H., Zhu, Z., Lu, Z., 2021. Effects of initial conditions on landing performance of the amphibious aircraft. *Acta*
 449 *Aeronautica et Astronautica Sinica* 42, 159–170. doi:10.7527/S1000-6893.2020.24483. (in Chinese).
- 450 Mei, X., Liu, Y., Yue, D.K.P., 1999. On the water impact of general two-dimensional sections. *Applied Ocean Research* 21, 1–15. doi:10.1016/
 451 S0141-1187(98)00034-0.
- 452 Neuberg, O., Drimer, N., 2017. Fatigue limit state design of fast boats. *Marine Structures* 55, 17–36. doi:10.1016/j.marstruc.2017.05.002.

- 453 Panciroli, R., Abrate, S., Minak, G., 2013. Dynamic response of flexible wedges entering the water. *Composite Structures* 99, 163–171.
 454 doi:10.1016/j.compstruct.2012.11.042.
- 455 Qiu, L., Song, W., 2013. Efficient decoupled hydrodynamic and aerodynamic analysis of amphibious aircraft water takeoff process. *Journal of*
 456 *Aircraft* 50, 1369–1379. doi:10.2514/1.C031846.
- 457 Qu, Q., Liu, C., Liu, P., Guo, B., Agarwal, R.K., 2016. Numerical simulation of water-landing performance of a regional aircraft. *Journal of Aircraft*
 458 53, 1680–1689. doi:10.2514/1.C033686.
- 459 Riccardi, G., Iafrati, A., 2004. Water impact of an asymmetric floating wedge. *Journal of Engineering Mathematics* 49, 19–39. doi:10.1023/B:
 460 ENGI.0000014885.89822.f5.
- 461 Russo, S., Jalalisedi, M., Falcucci, G., Porfiri, M., 2018. Experimental characterization of oblique and asymmetric water entry. *Experimental*
 462 *Thermal and Fluid Science* 92, 141–161. doi:10.1016/j.expthermflusci.2017.10.028.
- 463 Scolan, Y.M., Korobkin, A.A., 2001. Three-dimensional theory of water impact. part 1. inverse wagner problem. *Journal of Fluid Mechanics* 440,
 464 293–326. doi:10.1017/S002211200100475X.
- 465 Sheng, C., Yu, P., Wang, T., Chen, N., 2022. A cfd based kriging model for predicting the impact force on the sphere bottom during the early-water
 466 entry. *Ocean Engineering* 243, 110304. doi:10.1016/j.oceaneng.2021.110304.
- 467 Siemann, M.H., Schwinn, D.B., Scherer, J., Kohlgruber, D., 2017. Advances in numerical ditching simulation of flexible aircraft models.
 468 *International Journal of Crashworthiness* 23, 236–251. doi:10.1080/13588265.2017.1359462.
- 469 Siemann, M.N., Langrand, B., 2017. Coupled fluid-structure computational methods for aircraft ditching simulation: Comparison of ale-fe and
 470 sph-fe approaches. *Computers and Structures* 188, 95–108. doi:10.1016/j.compstruc.2017.04.004.
- 471 Terziev, M., Tezdogan, T., Incecik, A., 2022. Scale effects and full-scale ship hydrodynamics: A review. *Ocean Engineering* 245, 110496.
 472 doi:10.1016/j.oceaneng.2021.110496.
- 473 Vincent, L., Xiao, T., Yohann, D., Jung, S., Kanso, E., 2018. Dynamics of water entry. *Journal of Fluid Mechanics* 846, 508–535. doi:10.1017/
 474 jfm.2018.273.
- 475 Wagner, H., 1932. Phenomena associated with impacts and sliding on liquid surface. *Journal of Applied Mathematics and Mechanics* 12, 193–215.
 476 (in German).
- 477 Wang, J., Lugni, C., Faltinsen, O.M., 2015. Experimental and numerical investigation of a freefall wedge vertically entering the water surface.
 478 *Applied Ocean Research* 51, 181–203. doi:10.1016/j.apor.2015.04.003.
- 479 Wang, S., Gadelho, J., Islam, H., Soares, C.G., 2021a. Cfd modelling and grid uncertainty analysis of the free-falling water entry of 2d rigid bodies.
 480 *Applied Ocean Research* 115, 102813. doi:10.1016/j.apor.2021.102813.
- 481 Wang, S., Xiang, G., Soares, C.G., 2021b. Assessment of three-dimensional effects on slamming load predictions using openfoam. *Applied Ocean*
 482 *Research* 112, 102646. doi:10.1016/j.apor.2021.102646.
- 483 Wen, X., Liu, P., Qu, Q., Hu, T., 2020. Impact of wedge bodies on wedge-shaped water surface with varying speed. *Journal of Fluids and Structures*
 484 92, 102831. doi:10.1016/j.jfluidstructs.2019.102831.
- 485 Woodgate, M.A., Barakos, G.N., Scrase, N., Neville, T., 2019. Simulation of helicopter ditching using smoothed particle hydrodynamics. *Aerospace*
 486 *Science and Technology* 85, 277–292. doi:10.1016/j.ast.2018.12.016.
- 487 Wu, G.X., Sun, S.L., 2014. Similarity solution for oblique water entry of an expanding paraboloid. *Journal of Fluid Mechanics* 745, 398–408.
 488 doi:10.1017/jfm.2014.111.
- 489 Xiao, T., Lu, Y., Deng, S., Zhi, H., Zhu, Z., Chen, J., 2021a. Hydrodynamic characteristics of a helicopter ditching on different positions of wavy
 490 water. *Journal of Aircraft* 58, 1–12. doi:10.2514/1.C036186.
- 491 Xiao, T., Lu, Z., Deng, S., 2021b. Effect of initial pitching angle on helicopter ditching characteristics using sph method. *Journal of Aircraft* 58,
 492 167–181. doi:10.2514/1.C035898.
- 493 Xiao, T., Qin, N., Lu, Z., Sun, X., Tong, M., Wang, Z., 2017. Development of a smoothed particle hydrodynamics method and its application to
 494 aircraft ditching simulations. *Aerospace Science and Technology* 166, 28–43. doi:10.1016/j.ast.2017.02.022.
- 495 Yang, X., Ma, J., Wen, D., Yang, J., 2020. Crashworthy design and energy absorption mechanisms for helicopter structures: A systematic literature
 496 review. *Progress in Aerospace Sciences* 114, 100618. doi:10.1016/j.paerosci.2020.100618.
- 497 Yang, X.B., Xu, G.D., 2018. Numerical simulation of the oblique water entry of wedges with vortex shedding. *Brodogradnja* 69, 69–83.
 498 doi:10.21278/brod69406.
- 499 Yu, P., Shen, C., Zhen, C., Tang, H., Wang, T., 2019. Parametric study on the free-fall water entry of a sphere by using the rans method. *Journal of*
 500 *Marine Science and Engineering* 7, 122. doi:10.3390/jmse7050122.
- 501 Zekri, H.J., Korobkin, A.A., Cooker, M.J., 2021. Gravity effect on water entry during an early stage. *Journal of Fluid Mechanics* 916, A10.
 502 doi:10.1017/jfm.2021.190.
- 503 Zhao, R., Faltinsen, O.M., 1993. Water entry of two-dimensional bodies. *Journal of Fluid Mechanics* 246, 593–612. doi:10.1017/
 504 S002211209300028X.
- 505 Zheng, Y., Qu, Q., Liu, P., Wen, X., Zhang, Z., 2021. Numerical analysis of the porpoising motion of a blended wing body aircraft during ditching.
 506 *Aerospace Science and Technology* 119, 10731. doi:10.1016/j.ast.2021.10731.